Evidence of Rapid Phenocryst Growth of Olivine During Ascent in Basalts From the Big Pine Volcanic Field: Application of Olivine-Melt Thermometry and Hygrometry at the Liquidus

Sarah K. Brehm[1] (ID) **and Rebecca A. Lange[1]**

[1]Department of Earth and Environmental Sciences, University of Michigan, Ann Arbor, MI, USA

Abstract The Quaternary Big Pine (BP) volcanic field in eastern California is notable for the occurrence of mantle xenoliths in several flows. This points to rapid ascent of basalt through the crust and precludes prolonged storage in a crustal reservoir. In this study, the hypothesis of phenocryst growth during ascent is tested for several basalts (13–7 wt% MgO) and shown to be viable. Phenocrysts of olivine and clinopyroxene frequently display diffusion-limited growth textures, and clinopyroxene compositions are consistent with polybaric crystallization. When the most Mg-rich olivine in each sample is paired with the whole-rock composition, resulting $^{Fe^{2+}-Mg}K_D$(olivine-melt) values (0.31–0.36) match those calculated from literature models (0.32–0.36). Application of a Mg- and a Ni-based olivine-melt thermometer from the literature, both calibrated on the same experimental data set, leads to two sets of temperatures that vary linearly with whole-rock MgO wt%. Because the Ni thermometer is independent of water content, it provides the actual temperature at the onset of olivine crystallization (1247–1097°C), whereas the Mg thermometer gives the temperature under anhydrous conditions and thus allows ΔT ($= T_{Mg} - T_{Ni}$ = depression of liquidus due to water) to be obtained. The average ΔT for all samples is ~59°C, which is consistent with analyzed water contents of 1.5–3.0 wt% in olivine-hosted melt inclusions from the literature. Because the application of olivine-melt thermometry/hygrometry at the liquidus only requires microprobe analyses of olivine combined with whole-rock compositions, it can be used to obtain large global data sets of the temperature and water contents of basalts from different tectonic settings.

Plain Language Summary Basaltic lavas are a window into their mantle source regions, which is why it is important to determine their temperatures and water contents. In this study, a new approach that allows these two parameters to be quantified is demonstrated for basalts from the Big Pine volcanic field, CA. They were targeted because many contain chunks of dense mantle rocks, which precludes storage in a crustal magma chamber and points to direct ascent from the mantle to the surface along fractures. Two hypotheses are proposed, tested, and shown to be viable in this study: (1) olivine crystallized in the basalts during ascent, and (2) the most Mg-rich olivine analyzed in each basalt represents the first olivine to grow during ascent. This enables the most Mg-rich olivine to be paired with the whole-rock composition in the application of olivine-melt thermometry and hygrometry. The results match those from published, independent studies. The success of this approach paves the way for the attainment of large, high-quality data sets for basalts from a wide variety of tectonic settings. This, in turn, may allow global variations in mantle temperature and volatile content to be mapped in greater detail and better understood.

1. Introduction

High-Mg basalts are close approximations of partial melts of the mantle and have the potential to provide insights into mantle conditions at the time of melt segregation, including temperature, oxidation state, and water content. For example, numerous researchers have used high-Mg basalts to estimate mantle source temperatures (e.g., Asimow et al., 2001; Herzberg & Asimow, 2008; McKenzie & Bickle, 1988; Plank & Forsyth, 2016; Putirka, 2005; Putirka et al., 2007, 2018). These efforts require a priori knowledge regarding (i) mantle mineralogy, (ii) oxidation state, and (iii) the olivine-liquid Fe^{2+}-Mg exchange coefficient ($^{Fe^{2+}-Mg}K_D$ (olivine-melt)) under melt equilibration/segregation conditions. A complementary
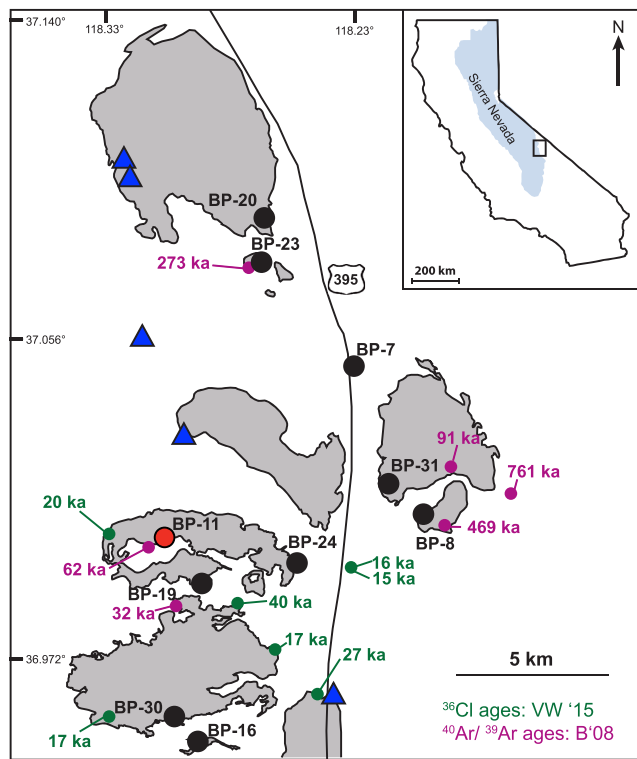
Figure 1. Map of the Quaternary Big Pine (BP) volcanic field adapted from Beard and Glazner (1995) and Vazquez and Woolford (2015). Gray regions are prominent basalt flows. Sample locations for this study are shown by solid circles. Triangles are localities of basalts with mantle xenoliths from Beard and Glazner (1995) and Wilshire et al. (1988). BP-11, shown in red (this study), contains a mantle xenolith. Cosmogenic ^{36}Cl ages and whole-rock ^{40}Ar/^{39}Ar ages are from Vazquez and Woolford (2015) and Blondes et al. (2008), respectively. The inset map shows the location of the Big Pine volcanic field along the western margin of the Basin and Range province.

approach is undertaken in this study, which is to constrain the temperature and water content of a basaltic melt *after* melt segregation, at the onset of olivine crystallization during ascent.

The primary question that is explored in this study is whether phenocryst growth in erupted basalts occurs during ascent along fractures and if evidence of their rapid crystallization can be readily identified through a series of tests. If so, a second question is whether the most Mg-rich olivine in each basalt can be used as a close approximation of the first olivine to crystallize from a melt with a composition similar to that of the whole rock. This study explores these two hypotheses, and in cases where they are shown to be viable, the most Mg-rich olivine in each sample is paired with the whole-rock composition to apply olivine-melt thermometry and hygrometry at the onset of olivine growth. Additionally, for basalts that are closely cosaturated with clinopyroxene at the onset of phenocryst growth, clinopyroxene-melt thermobarometry is also applied. For those basalts that contain plagioclase phenocrysts, minimum constraints on melt water contents at the onset of plagioclase growth are obtained.

In order to test the hypotheses of phenocryst growth during ascent and whether olivine-melt thermometry can be applied to the most Mg-rich olivine analyzed in each sample, basalts from the Quaternary Big Pine (BP) volcanic field in eastern California were targeted for four key reasons. First, the BP basalts are young (many are <500 ka; Blondes et al., 2007, 2008; Vazquez & Woolford, 2015), fresh, and well characterized in terms of their isotopic (e.g., Beard & Glazner, 1995; Beard & Johnson, 1997; Blondes et al., 2008; DePaolo & Daley, 2000) and major- and trace-element compositions (e.g., Blondes et al., 2008; Gazel et al., 2012; Ormerod et al., 1991; Putirka et al., 2012). Second, the presence of mantle xenoliths in several flows (e.g., Beard & Glazner, 1995; Ducea & Saleeby, 1996; Lee et al., 2001; Wilshire et al., 1988) indicates that their ascent through the crust was sufficiently rapid to overcome xenolith settling velocities (e.g., Sparks et al., 1977; Spera, 1980, 1984), which is consistent with phenocryst growth during ascent and not during prolonged storage in a crustal reservoir. Third, Fe^{3+}/Fe^T (Fe^T = total iron) ratios in olivine-hosted melt inclusions in BP basalts are known from μ-XANES (Kelley & Cottrell, 2012) and V-partitioning analyses (Gazel et al., 2012), which enables a test of whether the most Mg-rich olivine in each sample closely represents the first olivine to crystallize from the whole-rock liquid composition. Fourth, high-quality, published analyses of the water contents (1.5–3.0 wt%) in olivine-hosted melt inclusions in the BP basalts (Gazel et al., 2012) allow a test of the method applied in this study to constrain melt H_2O contents.

2. Geological Setting

The BP volcanic field, which is located in Owens Valley, California, along the eastern escarpment of the Sierra Nevada mountain range, sits along the western margin of the Great Basin, which has been undergoing lithospheric thinning (i.e., Basin and Range extension) since 12 Ma (e.g., Colgan et al., 2006; Henry & Perkins, 2002; Stockli et al., 2003). Prior to extension, the region was affected by Mesozoic subduction of the Farallon slab beneath the North American Plate (e.g., Christiansen & Lipman, 1972; Lipman et al., 1972; Snyder et al., 1976). The BP volcanic field resides on Precambrian continental lithosphere, east of the boundary with the Panthalassan terrane to the west (Kistler, 1990).

The BP volcanic field contains >20 Quaternary monogenetic vents (Figure 1) that erupted high-MgO (≤13 wt%) basalt; several flows contain mantle xenoliths (Beard & Glazner, 1995; Ducea & Saleeby, 1996; Lee et al., 2001; Wilshire et al., 1988). Mantle xenolith localities from Wilshire et al. (1988) and Beard and Glazner (1995) are shown in Figure 1. The BP volcanic field has been active since 1.2 Ma (Blondes et al., 2007, 2008), with the youngest eruptions (17, 27, and 40 ka) identified using cosmogenic ^{36}Cl dating (Vazquez &

Woolford, 2015). All BP basalts, regardless of age, have chondrite-normalized trace-element patterns that display enrichments in fluid-mobile elements (e.g., Ba), which is consistent with a subduction modified lithospheric mantle source (e.g., Blondes et al., 2008; Gazel et al., 2012; Ormerod et al., 1988, 1991; Putirka et al., 2012). Calculated depths of melt segregation in the literature range from 44–74 km (Putirka et al., 2012) to 30–80 km (Gazel et al., 2012).

3. Sample Locations and Petrography

Locations of the 10 basalt samples collected and examined in this study are shown in Figure 1; all are from eruptive vents <500 ka (Blondes et al., 2007, 2008; Vazquez & Woolford, 2015). In this study, a mantle xenolith (4 cm diameter) was discovered in Sample BP-11 (Figure 1). An image of the BP-11 mantle xenolith is presented in supporting information Figure S1. In two cases, two separate samples were obtained from different parts of the same flow (BP-11 and BP-24; BP-16 and BP-30; Figure 1). The objective of sampling two different parts of the same flow was to evaluate any variation in composition (whole-rock and phenocryst assemblage).

Phenocrysts of olivine ($\leq$2.7 mm) and clinopyroxene ($\leq$1.8 mm) are present in basalts with >9 wt% MgO, with plagioclase sparse to absent. The only exception is BP-7, where clinopyroxene is only found as microlites ($\leq$100 μm). Conversely, olivine and plagioclase are the dominant phenocrysts in the four low-MgO (7–8 wt%) basalts, with clinopyroxene sparse to absent. Olivine is the only phenocryst to contain inclusions of chromite. Titanomagnetite is present in the groundmass of all samples and occurs as inclusions in rims of zoned (sector/oscillatory) clinopyroxene phenocrysts. Ilmenite is only found in three samples (BP-7, BP-20, and BP-8) and is restricted to the groundmass.

Samples were evaluated for posteruptive alteration/oxidation through thin section examination. Two criteria were employed: (1) the presence of any iddingsite along the rims of olivine and (2) the presence of any alteration products in vesicles (for samples obtained along flow tops). Seven of the 10 BP samples are extremely fresh, with no evidence of any iddingsite rims on olivine. The remaining three (BP-7, BP-8, and BP-23) have trace to minor occurrences of iddingsite on some olivine crystals. Unfortunately, the sample that contains the mantle xenolith (BP-11; taken from a vesicular flow top) has alteration products in its vesicles, despite its pristine olivine (i.e., no trace of iddingsite); alteration in vesicles was not visible in the other samples.

4. Whole-Rock Basalt Compositions

4.1. Analytical Methods

Samples were crushed and powdered in a tungsten carbide shatter box and analyzed for major and trace elements. Efforts were made to avoid vesicle material in Sample BP-11 when powdering rock fragments. Major- and trace-element compositions were determined using inductively coupled plasma mass spectrometry (ICP-MS) at Activation Laboratories, Ontario, Canada. Samples were analyzed for bulk Ni content by single-element, pressed pellet X-ray fluorescence (XRF) at Activation Laboratories, Ontario, Canada. For each sample, whole-rock analyses of FeO wt% (Fe^{2+}) were obtained in duplicate by the Wilson (1960) titration method at the University of Michigan. Additionally, four FeO titration analyses were made on U.S. Geological Survey (USGS) standard W-2a to evaluate accuracy and reproducibility.

4.2. Results

All major-element oxide components are normalized to 100% and are presented in Table 1 with original totals and original loss on ignition (LOI). The BP basalts have variable MgO contents (7–13 wt%; Table 1) and are normative in nepheline (i.e., classify as alkali olivine basalts). Whole-rock Ni contents range from 76–343 ppm, and the average reproducibility on certified standards is $\pm$4 ppm. Note that the whole-rock compositions of the sample pairs taken from the same flow are very similar (BP-11 and BP-24; BP-16 and BP-30; Table 1). The full suite of analyzed trace-element concentrations for all samples are presented in Table S1. A chondrite-normalized (McDonough & Sun, 1995) trace-element diagram of the BP basalts compared to average Cascade arc basalt (Reiners et al., 2000) and an average Hawaiian tholeiite (Hofmann & Jochum, 1996) is presented in Figure S2. All samples display an arc geochemical signature (i.e., enrichment in fluid-mobile large ion lithophile elements, e.g., Ba) as previously noted in the literature (e.g., Blondes et al., 2008; Gazel et al., 2012; Ormerod et al., 1988, 1991; Putirka et al., 2012).

Table 1
Whole-Rock Major-Element (wt%) and Ni (ppm) Concentrations for Big Pine Basalts

	BP-23	BP-31	BP-11[a]	BP-19	BP-24	BP-7	BP-16	BP-30	BP-8	BP-20
Lat (N)	37°4.012′	37°1.03′	36°59.68′	36°58.84′	36°59.27′	37°3.29′	36°56.23′	36°56.65′	37°0.46′	37°5.31′
Long (W)	118°15.74′	118°12.81′	118°17.78′	118°17.02′	118°15.01′	118°13.78′	118°17.09′	118°17.60′	118°11.98′	118°15.72′
SiO_2	47.78	48.11	48.71	47.70	49.54	47.58	48.60	49.45	50.96	51.61
TiO_2	1.31	1.34	1.50	1.43	1.43	2.00	1.57	1.54	1.47	1.53
Al_2O_3	13.77	14.60	15.96	16.14	16.01	16.04	17.56	17.41	17.38	17.18
FeO^T	8.15	8.09	7.87	8.27	7.75	8.63	8.61	8.52	7.76	7.28
MnO	0.14	0.15	0.15	0.15	0.14	0.15	0.15	0.15	0.14	0.13
MgO	13.04	11.84	9.84	9.79	9.55	9.46	7.54	7.31	7.25	7.07
CaO	10.69	10.96	9.78	10.52	9.53	9.62	10.29	10.28	8.94	9.01
Na_2O	2.93	2.69	3.50	3.16	3.32	3.72	3.71	3.55	3.80	3.82
K_2O	1.26	1.40	1.91	1.81	1.92	1.73	1.07	1.03	1.57	1.63
P_2O_5	0.55	0.58	0.73	0.80	0.69	0.70	0.49	0.49	0.46	0.43
LOI	−0.37	−0.23	−0.06	−0.23	−0.11	−0.36	−0.40	−0.27	−0.27	−0.33
Total	100.0	100.3	99.8	99.8	99.6	99.6	99.8	100.2	100.3	100.2
Ni (ppm)	343	268	201	156	188	177	82	76	83	95
Mg#[b]	0.79	0.77	0.75	0.74	0.74	0.72	0.67	0.67	0.69	0.70
					$Fe^{2+}O$ wt% titrations (Wilson, 1960)[c]					
$Fe^{2+}O$ wt%	6.33	6.19	*5.13*	6.16	5.74	6.69	*6.00*	5.97	5.69	6.01
Fe^{3+}/Fe^T	0.22	0.23	*0.35*	0.26	0.26	0.22	*0.30*	0.30	0.27	0.17

Note. Major-element analyses normalized to 100%, presented with LOIs and original totals. Values from BP-11 and BP-16 are italicized to reflect alteration or sample heterogeneity. [a]BP-11 (mantle xenolith bearing) contains alteration products in its vesicles. [b]Mg# $= X_{MgO}/(X_{MgO} + X_{FeO})$ calculated using $Fe^{3+}/Fe^T = 0.241$ (average μ-XANES, Kelley & Cottrell, 2012). [c]Average of duplicate $Fe^{2+}O$ wt% (and resulting Fe^{3+}/Fe^T) measurements using the Wilson (1960) titration method (Table S2).

The average (±1 s.d.) of four analyses of wt% FeO (ferrous iron concentration) for the USGS standard (W-2a) is 8.44 (±0.22) wt%, in agreement with the certified value of 8.34 ± 0.09 wt%. The results of individual titrations on the BP samples and the standard (W-2a) are presented in Table S2. The average wt% FeO analyzed for each sample is given in Table 1, together with resulting whole-rock Fe^{3+}/Fe^T ratios. Note that the xenolith-bearing sample, BP-11, was obtained from a flow top with visible alteration products in its vesicles. Although attempts were made to avoid altered material during crushing and powdering, the Fe^{3+}/Fe^T value for BP-11 may reflect the effects of alteration and is not considered a magmatic value. Similarly, for BP-16 (also a highly vesicular sample), the duplicate wt% FeO analyses were different outside of expected analytical error (1 s.d. = ±0.51 wt% FeO), which points to heterogeneity that may reflect the presence of some vesicle alteration material; its Fe^{3+}/Fe^T value was likely affected. For all other samples, the Fe^{3+}/Fe^T values based on whole-rock analyses range from 0.17–0.30, with an average (±1σ) value of 0.24 (±0.04). Therefore, within analytical error, the unaltered whole-rock Fe^{3+}/Fe^T ratios are close to those obtained from olivine-hosted melt inclusions in the BP basalts by direct μ-XANES analyses (0.24–0.25; Kelley & Cottrell, 2012) and V-partitioning calculations (0.23–0.30; Gazel et al., 2012).

5. Mineral Compositions

5.1. Electron Microprobe Analytical Methods

Compositional analyses of olivine, clinopyroxene, plagioclase, and Fe-Ti oxides were obtained using a Cameca SX-100 electron microprobe at the Robert B. Mitchell Electron Microbeam Analysis Lab at the University of Michigan. The microprobe standards used for each element in each phase are presented in Table S3.

For olivine, two beam conditions were used to analyze eight elements (Mg, Al, Si, Ca, Cr, Mn, Fe, and Ni). In the first set, an accelerating voltage of 15 kV, a focused beam of 20 nA, and individual peak and background counting times of 20 s were used. The 1σ uncertainty for each oxide based on counting statistics is ±0.45 wt% SiO_2, ±0.35 wt% MgO, ±0.56 wt% FeO^T, ±0.05 wt% NiO, ±0.03 wt% Al_2O_3, ±0.03 wt% CaO, ±0.04 wt% Cr_2O_3, and ±0.11 wt% MnO. Analytical transects across 574 different olivine crystals (30 to 105 per

sample) ($\leq$2.7 mm) were performed. Data were obtained every 20 to 40 μm, yielding between 266 and 1,328 olivine analyses per sample.

In the second set of beam conditions, designed to increase the precision of the Ni analyses, an accelerating voltage of 20 kV and a 40 nA current was used. Background and peak counting times were 20 s for Al, Mn, Cr, and Ca, whereas peak and background counting times of 30 and 20 s, respectively, were used for Si, Mg, Fe, and Ni. The 1σ uncertainty for each oxide based on counting statistics is $\pm$0.36 wt% SiO_2, $\pm$0.24 wt% MgO, $\pm$0.24 wt% FeO^T, $\pm$0.02 wt% NiO, and less than <0.1 wt% for Cr_2O_3, Al_2O_3, MnO, and CaO. This second set of beam conditions was used to reanalyze transects along two to three of the most Mg-rich olivine crystals from each sample as well as olivine grains in the mantle xenolith from BP-11. Approximately 50 analyses were obtained on olivine crystals in the mantle xenolith. Additionally, a mantle xenolith olivine from the San Carlos volcanic field (AZ) was analyzed for comparison. All olivine analyses were filtered to exclude those with totals outside of 99–101 wt%.

Analyses of clinopyroxene were obtained for the six BP basalts with >9 wt% MgO (Table 1) (i.e., those with clinopyroxene phenocrysts). However, in Sample BP-7, clinopyroxene was only found as microlites (<100 μm) in the groundmass. Ten elements (Na, Mg, Al, Si, Ca, Ti, Cr, Mn, Fe, and Ni) were analyzed using an accelerating potential of 20 kV and a focused 20 nA beam current with individual peak and background counting times of 20 s. Single analytical transects were acquired for 357 individual clinopyroxene crystals (5–140 per sample). Additional transects were collected for phenocrysts where complex chemical zonation (i.e., oscillatory, sector, and distinct cores) was observed via backscattered electron (BSE) imaging. The 1σ uncertainty for each oxide based on counting statistics is $\pm$0.04 wt% Na_2O, $\pm$0.18 wt% MgO, $\pm$0.13 wt% Al_2O_3, $\pm$0.40 wt% SiO_2, $\pm$0.24 wt% CaO, $\pm$0.06 wt% TiO_2, $\pm$0.04 wt% Cr_2O_3, $\pm$0.03 wt% MnO, $\pm$0.12 wt% FeO^T, and $\pm$0.03 wt% NiO. Analytical totals were filtered to exclude those outside of 98.5–100.5 wt%. In one sample (BP-31), olivine inclusions in clinopyroxene were analyzed using the same beam conditions for clinopyroxene. Additional details on the standards used for these olivine analyses are presented in Table S3.

Plagioclase analyses were obtained on the four low-MgO basalt samples (Table 1). For these analyses, a 15 kV accelerating potential with a focused 4 nA beam was used to analyze nine elements (Mg, Na, Si, Al, Ti, Fe, Mn, Ca, and K) with individual peak and background counting times of 20 s. Transects of 90 plagioclase crystals (13 to 34 per sample) (185 μm to 1.4 mm) were performed, yielding between 237 and 415 analyses per sample. Plagioclase analyses were filtered to exclude analytical totals outside 98.5 and 101 wt%. The 1σ uncertainty for each oxide based on counting statistics is $\pm$0.23 wt% Na_2O, $\pm$0.06 wt% MgO, $\pm$0.75 wt% Al_2O_3, $\pm$0.98 wt% SiO_2, $\pm$0.09 wt% K_2O, $\pm$0.52 wt% CaO, $\pm$0.08 wt% MnO, $\pm$0.14 wt% FeO^T, and $\pm$0.06 wt% TiO_2.

Three samples from this study (BP-7, BP-8, and BP-20) contain both ilmenite and titanomagnetite. In all other samples, ilmenite is absent. For Fe-Ti oxide analyses, a focused beam with an accelerating voltage of 15 kV and a 10 nA beam current was used. Nine elements (Si, Ti, Al, Fe, V, Cr, Mn, Mg, and Ca) were analyzed with individual peak and background counting times of 20 s. The ilmenite 1σ uncertainty based on counting statistics is $\pm$0.14 wt% MgO, $\pm$0.06 wt% Al_2O_3, $\pm$0.06 wt% SiO_2, $\pm$0.05 wt% CaO, $\pm$0.77 wt% V_2O_3, $\pm$0.09 wt% Cr_2O_3, $\pm$0.05 wt% MnO, $\pm$0.09 wt% FeO^T, and $\pm$0.83 wt% TiO_2. The titanomagnetite 1σ uncertainty based on counting statistics is $\pm$0.13 wt% MgO, $\pm$0.10 wt% Al_2O_3, $\pm$0.06 wt% SiO_2, $\pm$0.05 wt% CaO, $\pm$0.42 wt% V_2O_3, $\pm$0.09 wt% Cr_2O_3, $\pm$0.05 wt% MnO, $\pm$0.09 wt% FeO^T, and $\pm$1.10 wt% TiO_2. Fe-Ti oxide analyses were filtered to discard those with $\geq$0.25 wt% SiO_2 and CaO and totals outside 98–101 wt%. FeO and Fe_2O_3 were calculated based on cation stoichiometry. Successful analyses of both ilmenite and titanomagnetite were only obtained for BP-20.

5.2. X-ray Intensity Mapping Methods (and BSE Images)

X-ray intensity maps of phosphorous (P) and iron (Fe) were obtained for the most Mg-rich olivine crystals in each of six BP basalts (BP-23, BP-31, BP-11, BP-19, BP-24, and BP-7). A 20 kV accelerating voltage and 200 nA beam current were utilized with dwell times of 200–300 μs/pixel. For comparison, similar maps were obtained on the olivine crystal from the San Carlos mantle xenolith. In one of these samples (BP-31), X-ray intensity maps of Mg, as well as aluminum (Al) and chromium (Cr), were obtained for a representative clinopyroxene phenocryst using a 15 kV accelerating voltage and 500 nA beam current with a dwell time of 200 μs/pixel. BSE images were obtained for all analyzed olivine and clinopyroxene crystals.
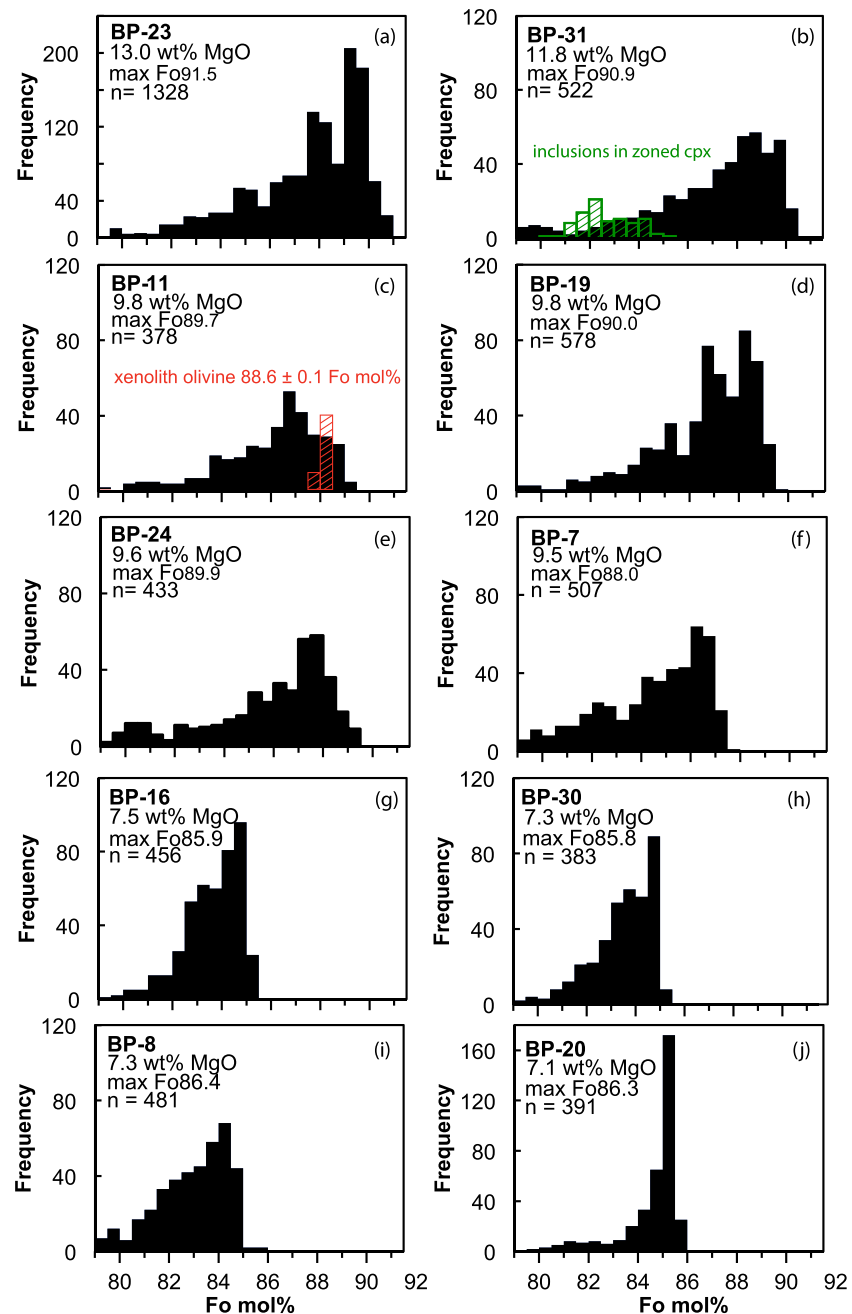
Figure 2. (a–j) Histograms of forsterite (Fo mol% = $X_{\text{MgO}}/(X_{\text{MgO}} + X_{\text{FeO}}) \times 100$) content of olivine crystals in 10 BP basalts. The most Fo-rich olivine compositions are reported in Table 2 (all analyses reported in Table S4). Whole-rock MgO wt%, maximum Fo analyzed, and number of analyses (n) are given for each sample. Fo contents for analyzed olivine in mantle xenolith (BP-11) are shown in red and overlap Fo contents of olivine phenocrysts. Fo contents for analyzed olivine inclusions in sector- or oscillatory-zoned clinopyroxene crystals in BP-31 are shown in green.

5.3. Olivine Results

Individual analyses of olivine crystals in each BP sample (as well as those for the olivine in the mantle xenolith in BP-11 and the San Carlos olivine) are given in Table S4 and summarized in histograms of mol% forsterite (Figure 2). The results show a continuous range in composition up to the most Mg-rich olivine in each sample (Table 2 and Figure 2). Plots of analyzed NiO wt% and CaO wt% as a function of mol% forsterite (Fo) for each sample are shown in Figures 3 and 4, respectively. Plots of analyzed CaO wt% (Figure 4) show that

Table 2
Composition of the Most Mg-Rich Olivine and Thermometry Results at the Onset of Phenocryst Growth

Oxide wt%	BP-23	BP-31	BP-11	BP-19	BP-24	BP-7	BP-16	BP-30	BP-8	BP-20	BP-11 xenolith	San Carlos, AZ
SiO_2	41.68	41.44	41.19	41.39	41.72	40.45	40.14	39.84	41.27	40.24	41.31	41.50
Al_2O_3	0.04	0.03	0.08	0.04	0.05	0.05	0.42	0.10	0.05	0.08	0.04	0.02
FeO	8.16	8.72	9.72	9.65	9.63	11.27	13.47	13.75	12.83	12.99	10.72	8.86
MnO	0.11	0.12	0.18	0.15	0.14	0.14	0.20	0.22	0.20	0.17	0.16	0.11
MgO	49.38	48.96	47.68	48.82	48.04	46.55	45.92	46.56	45.81	46.03	47.71	49.22
Cr_2O_3	0.08	0.08	0.07	0.05	0.06	0.07	0.00	0.01	0.02	0.03	0.02	0.04
NiO[a]	0.42	0.35	0.34	0.31	0.33	0.31	0.20	0.20	0.26	0.25	[0.32][b]	[0.41][b]
CaO[a]	0.20	0.24	0.22	0.22	0.22	0.22	0.21	0.21	0.20	0.19	[0.02][b]	[0.04][b]
Total	100.1	99.9	100.1	100.6	100.2	99.1	100.6	100.9	100.7	100.0	100.4	100.3
Fo mol%[c]	91.5	90.9	89.7	90.0	89.9	88.0	85.9	85.8	86.4	86.3	88.8	90.8
Fe^{2+}-$^{Mg}K_D$ liquidus test[d]	0.35	0.34	0.34	0.31	0.33	0.35	0.34	0.33	0.35	0.36		
Olivine-melt thermometry (Pu et al., 2017)												
T_{Mg} (°C)[e]	1309 ± 4	1281 ± 4	1249 ± 5	1238 ± 5	1242 ± 5	1240 ± 5	1182 ± 5	1171 ± 5	1189 ± 5	1182 ± 5		
T_{Ni} (°C) (recommended)[e]	1247 ± 12	1238 ± 15	1198 ± 14	1159 ± 15	1211 ± 14	1186 ± 16	1122 ± 23	1124 ± 23	1097 ± 18	1132 ± 19		
$\Delta T = T_{Mg} - T_{Ni}$ (°C)[e]	63 ± 13	43 ± 16	51 ± 15	79 ± 16	32 ± 15	54 ± 17	60 ± 24	47 ± 24	93 ± 19	50 ± 20		
$D_{Ca}^{ol/liq}$ mol%	0.0153	0.0172	0.0179	0.0166	0.0185	0.0181	0.0160	0.0161	0.0170	0.0170		
Olivine-melt thermometry (Putirka et al., 2007)												
T_{Mg} anhydrous (°C)[f]	1309	1281	1246	1238	1238	1240	1185	1174	1185	1178		
T_{Mg} (°C), 1.5 wt% H_2O[f]	1273	1246	1213	1206	1206	1208	1156	1145	1155	1148		
T_{Mg} (°C), 3.0 wt% H_2O[f]	1238	1213	1182	1175	1175	1177	1127	1117	1127	1120		

[a]NiO and CaO wt% from linear fits in Figures 4 and 5, respectively. [b]Analyzed. [c]Fo mol% = $X_{MgO}/(X_{MgO} + X_{FeO}) \times 100$. [d]Calculated from Equation 1 using most Mg-rich olivine and whole-rock composition ($Fe^{3+}/Fe^T = 0.24$; Kelley & Cottrell, 2012). [e]T_{Mg}, T_{Ni}, and ΔT calculated according to the model of Pu et al. (2017); errors are propagated from analytical uncertainty. [f]T_{Mg} calculated according to the model of Putirka et al. (2007), which contains a correction for melt H_2O wt%.
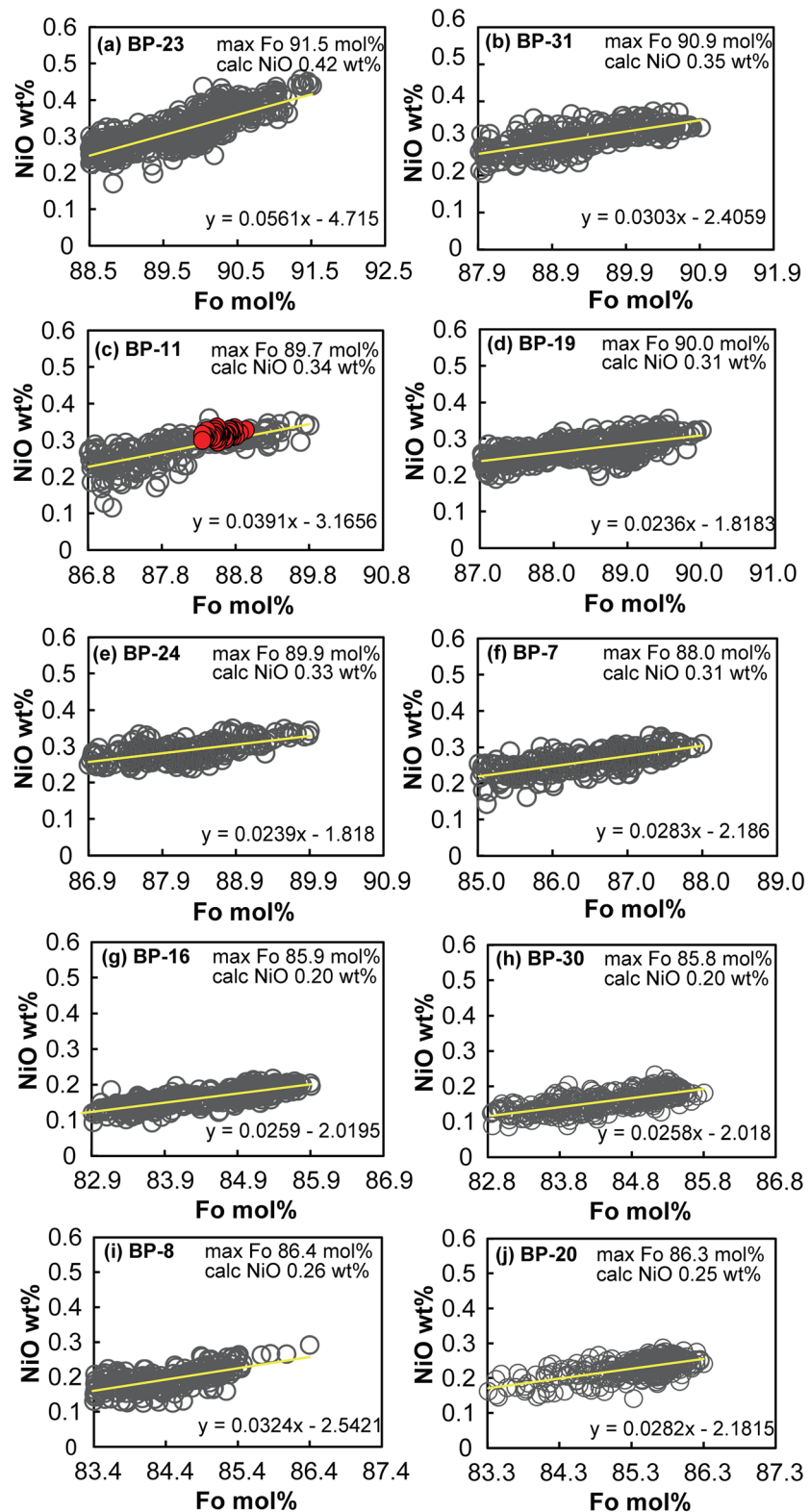
Figure 3. (a–j) wt% NiO in olivine versus Fo mol% = $(X_{MgO}/(X_{MgO} + X_{FeO})) \times 100$ for olivine analyses that span the highest 3 mol% Fo in each sample. A linear fit to the data (yellow line) is used to calculate wt% NiO for the most Fo-rich olivine in each sample, which is used in the Ni thermometer. BP-11 mantle xenolith olivines are shown in red for comparison. The most Fo-rich olivine composition and calculated NiO wt% are labeled on each plot and reported in Table 2.
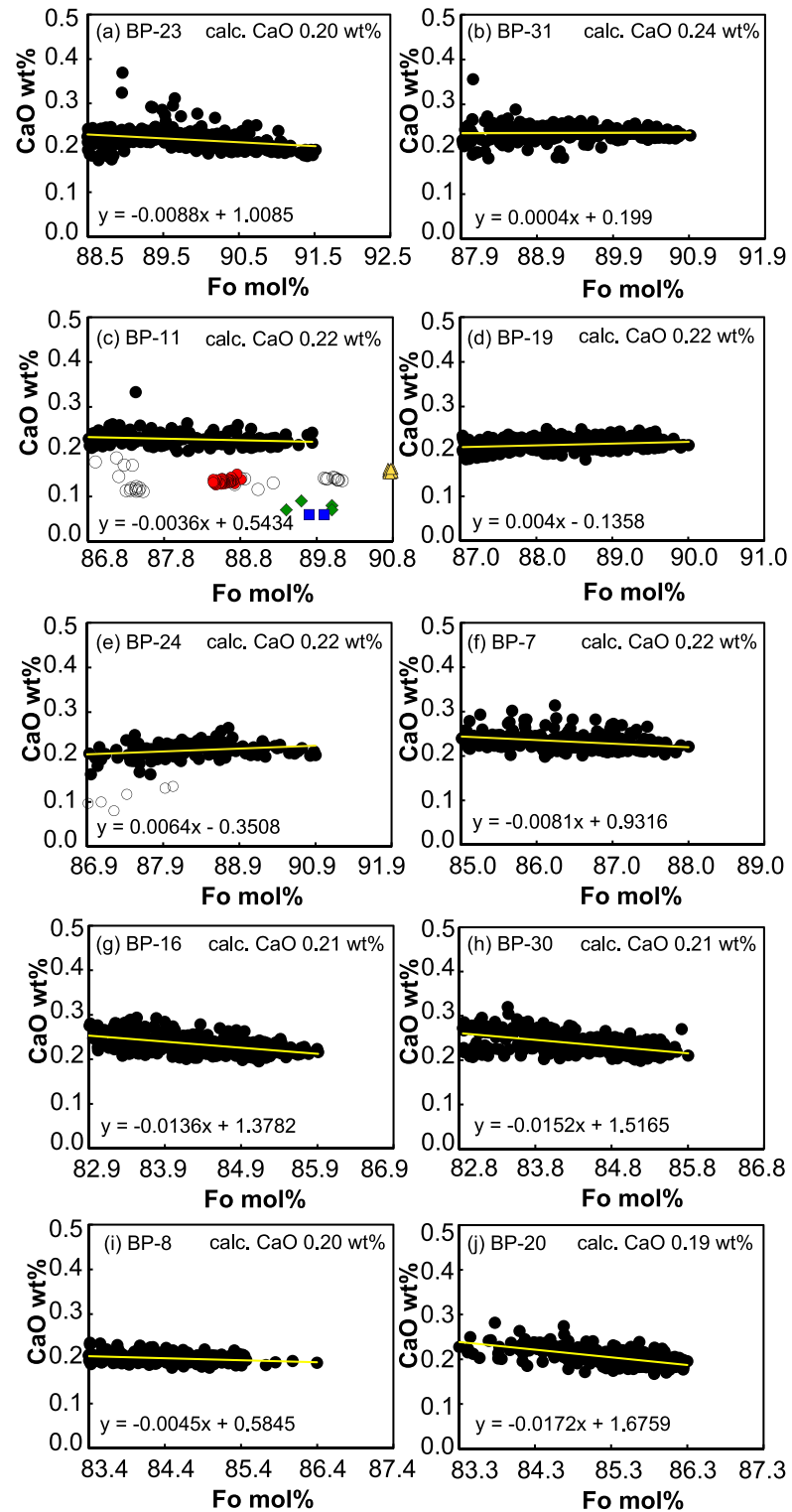
Figure 4. (a–j) CaO wt% in olivine versus Fo mol% for olivines that span the top 3 mol% Fo in each sample. A linear fit to the top 3 mol% is shown on each plot in yellow and is used to calculate CaO wt% for the most Mg-rich olivine. Olivine phenocrysts (black) have systematically higher CaO wt% compared to mantle xenolith olivine analyzed in BP-11 (red). CaO wt% in olivine from other BPVF mantle xenoliths is shown in blue (Beard & Glazner, 1995) and green (Wilshire et al., 1988). Analyses of mantle olivine from San Carlos, AZ, xenoliths are shown for comparison in yellow. All mantle olivine analyses have ≤0.15 wt% CaO (e.g., Housh et al., 2010; Norman & Garcia, 1999; Simkin & Smith, 1970), which is used to identify possible olivine xenocrysts from mantle xenoliths (open symbols).

the dominant olivine population in each sample contains >0.15 wt% CaO, whereas a sparse subset in two samples (BP-11 and BP-24) contains ≤0.15 wt% CaO. For both NiO and CaO analyses, data that span the highest three mol% Fo are fitted to a linear relationship for each sample, which is used to calculate the NiO and CaO wt% in the most Mg-rich olivine. Application of the linear fit reduces the scatter due to analytical error and allows a more accurate estimate of both the NiO and CaO contents in the most Mg-rich olivine (Table 2) in each sample.

In the BP-11 mantle xenolith, the average analyzed olivine composition is 88.8 ± 0.1 Fo mol%, 0.32 ± 0.01 NiO wt%, and 0.13 ± 0.004 wt% CaO (Table 2). Both the forsterite content (Figure 2c) and the NiO wt% (Figure 3c) in olivines from the mantle xenolith overlap those observed in olivine phenocrysts from BP-11, whereas the CaO contents are distinctly lower than those in the phenocrysts (Figure 4). Olivine crystals from BP mantle xenoliths from two previous studies (Beard & Glazner, 1995; Lee et al., 2001), as well as olivine crystals from San Carlos mantle xenoliths, are also lower in CaO relative to phenocrysts of olivine (Figure 4c). The low-CaO character of olivine from mantle peridotites has long been noted in the literature (e.g., Simkin & Smith, 1970; Norman & Garcia, 1999; Housh et al., 2010). In this study, a filter of <0.15 wt% CaO was applied to identify any low-Ca olivine in the BP samples (Figure 4). The sparse population of low-CaO olivine crystals (e.g., BP-11 and BP-24; Figure 4) are interpreted as disaggregated olivine xenocrysts from mantle xenoliths.

X-ray intensity maps of P and Fe for the most Mg-rich olivine crystal in each of six BP basalts are shown in Figure 5. All samples contain olivine crystals that display complex P zoning patterns. For comparison, a P map of an olivine from a mantle xenolith (San Carlos, AZ) shows no zones of P enrichment (Figure 5n). BSE images of representative olivine phenocrysts from six other BP basalts are shown in Figure 6.

5.4. Clinopyroxene Results

All individual analyses of clinopyroxene from the six high-MgO (>9 wt%) BP basalts are tabulated in Table S5. Compositions for the most Mg-rich clinopyroxene crystal in each sample are presented in Tables 3 and 4. In Figure 7, plots of Na_2O (wt%) versus Mg# show two distinct compositional trends, whereas plots of TiO_2 (wt%) versus Mg# primarily follow a continuous compositional range among the clinopyroxene phenocrysts in each of four samples (BP-23, BP-31, BP-11, and BP-19). Similar data for BP-7 (no phenocrysts, only microlites) and BP-24 (sampled from same flow as BP-11) are shown in Figure S3. The analyses in Figure 7 are given different symbols based on the texture observed for each analytical spot along a transect: (1) nonspongy (nonvermicular), (2) spongy (vermicular), and (3) sector and/or oscillatory zoned. Examples of all three clinopyroxene textures from these four samples are shown in BSE images (Figure 8). In all cases, the clinopyroxene analyses with the highest Na_2O content (and lowest TiO_2) content have the nonspongy (nonvermicular) texture (Figures 7 and 8a–8d). The spongy (vermicular) texture is found across the compositional continuum (Figures 7 and 8e–8h). Importantly, most sector- and/or oscillatory-zoned analyses plot in the low-Na_2O and high-TiO_2 group (Figures 7 and 8i–8l).

The relative abundance of the three clinopyroxene textures in each of the four basalt samples is qualitatively illustrated in a histogram of Mg# (Figure 9). BP-23 contains the highest abundance of nonspongy, high-Na_2O, and low-TiO_2 clinopyroxene, whereas BP-31 contains the most oscillatory and sector zoned (all low Na_2O), with few analyses with the nonspongy texture. For one of the zoned clinopyroxene phenocrysts from BP-31 (cpx-1; Figures 7c and 7d), X-ray intensity maps (Figure 10) show that sector zoning strongly affects Al and Mg concentrations, but not Cr contents; in contrast, all three elements display marked oscillatory zonation in this same crystal. Note that analyses obtained on this single crystal (cpx-1) span the entire compositional range as those for all oscillatory- and sector-zoned clinopyroxene phenocrysts in BP-31 (Figures 7c and 7d).

5.5. Plagioclase Results

Individual plagioclase analyses of phenocrysts from the four low-MgO BP samples are tabulated in Table S6. The analyses are summarized for each sample in histograms of mol% anorthite (An) in Figure S4. The most calcic plagioclase composition in each sample is highlighted in Table S6. Each of the four samples contains a plagioclase phenocryst population that spans a continuous compositional range up to approximately An_{75-76}.
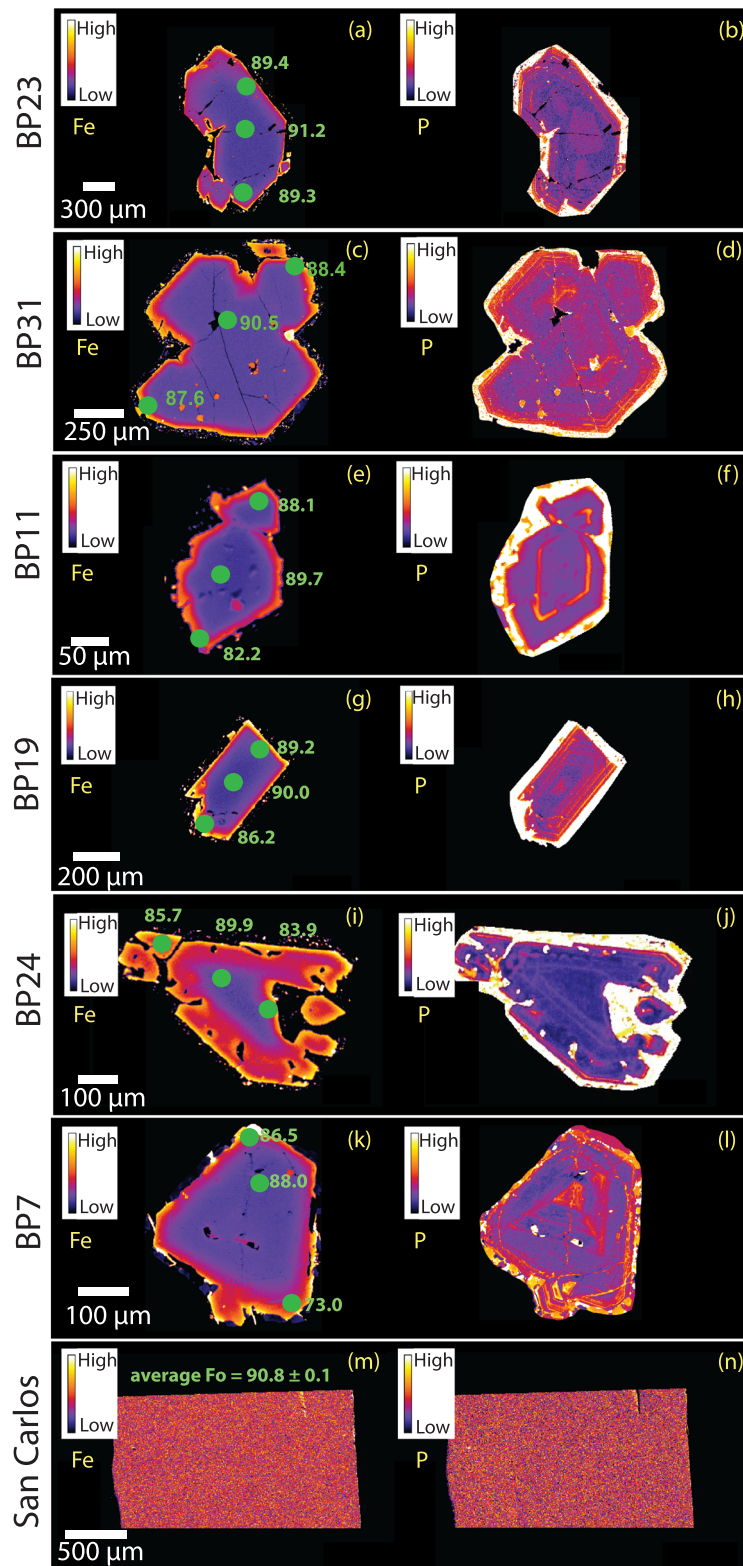
Figure 5. X-ray intensity maps of Fe (a, c, e, g, i, k, m) and P (b, d, f, h, j, l, n) for the most Fo-rich olivine analyzed, respectively, in six BP samples. Analytical spots and the associated Fo mol% are shown in green. X-ray maps of a mantle xenolith olivine from San Carlos, Arizona, are shown for comparison. Complex P zoning in olivine phenocrysts from BP basalts is consistent with an initial period of diffusion-limited rapid growth (e.g., Milman-Barris et al., 2008; Shea et al., 2019; Welsch et al., 2012, 2014).
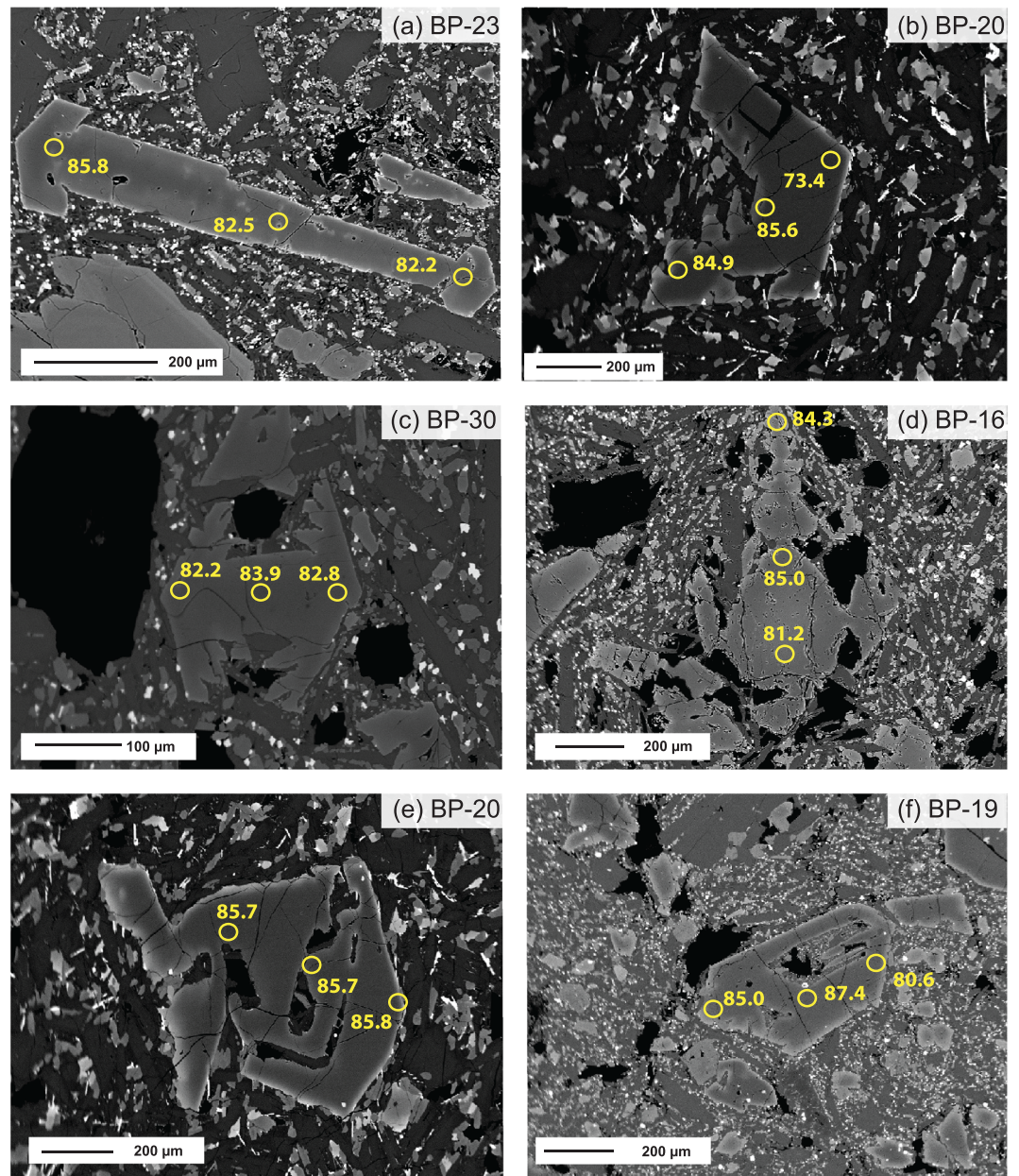
Figure 6. Representative backscattered electron images of olivine phenocrysts that display diffusion-limited growth textures from six BPVF basalts. Fo content (mol%) spot analyses are shown in yellow.

5.6. Fe-Ti Oxide Results

Individual analyses of ilmenite and titanomagnetite crystals for BP-20 are presented in Table S7. The Bacon and Hirschmann (1988) Mg/Mn equilibrium test was applied to all possible ilmenite-titanomagnetite pairs in order to discern those that could have cocrystallized together. The results indicate six viable equilibrium pairs, which are reported in Table S7. Temperature and oxygen fugacity values were calculated for each ilmenite-titanomagnetite pair that passed the Bacon and Hirschmann (1988) equilibrium test (Table S7) using the model of Ghiorso and Evans (2008). The thermometry results (980–840°C) are consistent with cocrystallization of both Fe-Ti oxides syneruptively in the groundmass. At the onset of ilmenite-titanomagnetite cocrystallization at ~980°C, the ΔNNO value was −0.45, which is consistent with a melt Fe^{3+}/Fe^{T} ratio intermediate between that at QFM (~0.16) and NNO (~0.21), namely, ~0.19.

Table 3

Effect of $^{Fe^{2+}-Mg}K_D$(Olivine-Melt) Values From the Literature on Olivine-Melt Oxybarometry Results

	BP-23	BP-31	BP-11	BP-19	BP-24	BP-7	BP-16	BP-30	BP-8	BP-20
				Calc. $^{Fe^{2+}-Mg}K_D$ (olivine-melt) values from literature					
MELTS[a]	0.34	0.35	0.34	0.34	0.34	0.32	0.32	0.33	0.33	0.34
MELTS + 0.01[a]	0.35	0.36	0.35	0.35	0.35	0.33	0.33	0.34	0.34	0.35
Putirka (2016)[b]	0.33	0.33	0.33	0.33	0.33	0.33	0.33	0.33	0.33	0.33
Putirka (2016) + 0.01[b]	0.34	0.34	0.34	0.34	0.34	0.34	0.34	0.34	0.34	0.34
Average	0.34	0.35	0.34	0.34	0.34	0.33	0.33	0.34	0.34	0.34
1σ	0.01	0.01	0.01	0.01	0.01	0.01	0.01	0.01	0.01	0.01
				Calc. melt Fe^{3+}/Fe^T ratios using olivine-melt oxybarometry[c]					
MELTS	0.23	0.25	0.23	0.30	0.27	0.16	0.20	0.23	0.22	0.20
MELTS + 0.01	0.25	0.27	0.26	0.32	0.30	0.19	0.22	0.25	0.24	0.23
Putirka (2016)	0.20	0.21	0.23	0.29	0.25	0.19	0.22	0.23	0.22	0.18
Putirka (2016) + 0.01	0.22	0.24	0.23	0.30	0.27	0.21	0.25	0.26	0.23	0.20
Average	0.23	0.24	0.24	0.30	0.27	0.19	0.22	0.24	0.23	0.20
1σ	0.02	0.03	0.02	0.01	0.02	0.02	0.02	0.02	0.01	0.02
				Calc. whole-rock $Fe^{2+}O$ wt%[d]					
MELTS	6.25	6.05	6.02	5.81	5.65	7.26	6.89	6.60	6.07	5.81
MELTS + 0.01	6.09	5.88	5.83	5.62	5.41	7.01	6.68	6.40	5.89	5.64
Putirka (2016)	6.53	5.87	6.08	5.87	5.80	7.03	6.70	6.53	6.07	5.99
Putirka (2016) + 0.01	6.31	6.11	6.02	5.75	5.65	6.82	6.50	6.31	5.93	5.81
Average	6.30	5.98	5.99	5.76	5.63	7.03	6.69	6.46	5.99	5.81
1σ	0.18	0.12	0.11	0.11	0.16	0.18	0.16	0.13	0.09	0.14
				$Fe^{2+}O$ wt% titrations[e]					
$Fe^{2+}O$ wt%	6.33	6.19	5.13	6.16	5.74	6.69	6.00	5.97	5.69	6.01
$\Delta Fe^{2+}O$[f]	0.04	0.21	−0.86	0.40	0.11	−0.34	−0.69	−0.49	−0.30	0.20

[a]$^{Fe^{2+}-Mg}K_D$(olivine-melt) from MELTS (Asimow & Ghiorso, 1998; Ghiorso & Sack, 1995) run anhydrous and $\Delta NNO = 0$; +0.01 is added to account for presence of H_2O (see text). [b]$^{Fe^{2+}-Mg}K_D$(olivine-melt) from Putirka (2016); +0.01 added to account for presence of H_2O (see text). [c]Melt Fe^{3+}/Fe^T ratios are calculated using the most Mg-rich olivine composition, the whole-rock composition, and calc. $^{Fe^{2+}-Mg}K_D$(olivine-melt) from the literature (MELTS; Putirka, 2016). [d]Calculated whole-rock $Fe^{2+}O$ wt% using melt Fe^{3+}/Fe^T results from olivine-melt oxybarometry. [e]Average of duplicate $Fe^{2+}O$ wt% (and resulting Fe^{3+}/Fe^T) measurements using the Wilson (1960) titration method (Table S2). [f]$\Delta Fe^{2+}O = Fe^{2+}O$ (titrations) − $Fe^{2+}O$ (avg. olivine-melt oxybarometry).

Table 4

Max Mg# Clinopyroxene Composition (wt%) and cpx-Liquid Barometry

Oxide wt%	BP-23	BP-31	BP-11	BP-19	BP-24
Crystal	cpx-28	cpx-80a	cpx-31	cpx-10	cpx-1
SiO_2	52.03	51.53	49.54	51.58	51.35
TiO_2	0.30	0.28	0.57	0.27	0.54
Al_2O_3	3.28	4.39	6.01	4.39	4.91
Cr_2O_3	0.93	0.63	1.13	1.13	0.55
FeO	3.40	3.81	4.16	4.12	4.02
MnO	0.09	0.10	0.11	0.13	0.08
MgO	17.94	18.00	16.60	18.98	17.14
CaO	21.50	20.62	20.48	19.39	21.04
Na_2O	0.51	0.44	0.59	0.48	0.45
NiO	0.02	0.03	0.06	0.03	0.04
Total	100.00	99.83	99.25	100.49	100.11
Mg#	90.4	89.4	87.7	89.1	88.4
			Clinopyroxene-liquid barometry[a]		
$^{Fe^T-Mg}K_D$ (cxp-liq)	0.30	0.31	0.31	0.26	0.29
P (GPa), T_{Ni}[b]	0.73	0.73	0.89	0.77	0.69
Depth (km)[c]	27	27	33	28	26

[a]Calculated with Neave and Putirka (2017) model; whole rock for liquid composition. [b]T_{Ni} from Table 2. [c]Average crustal density of 2.75 g/cm^3 is assumed.
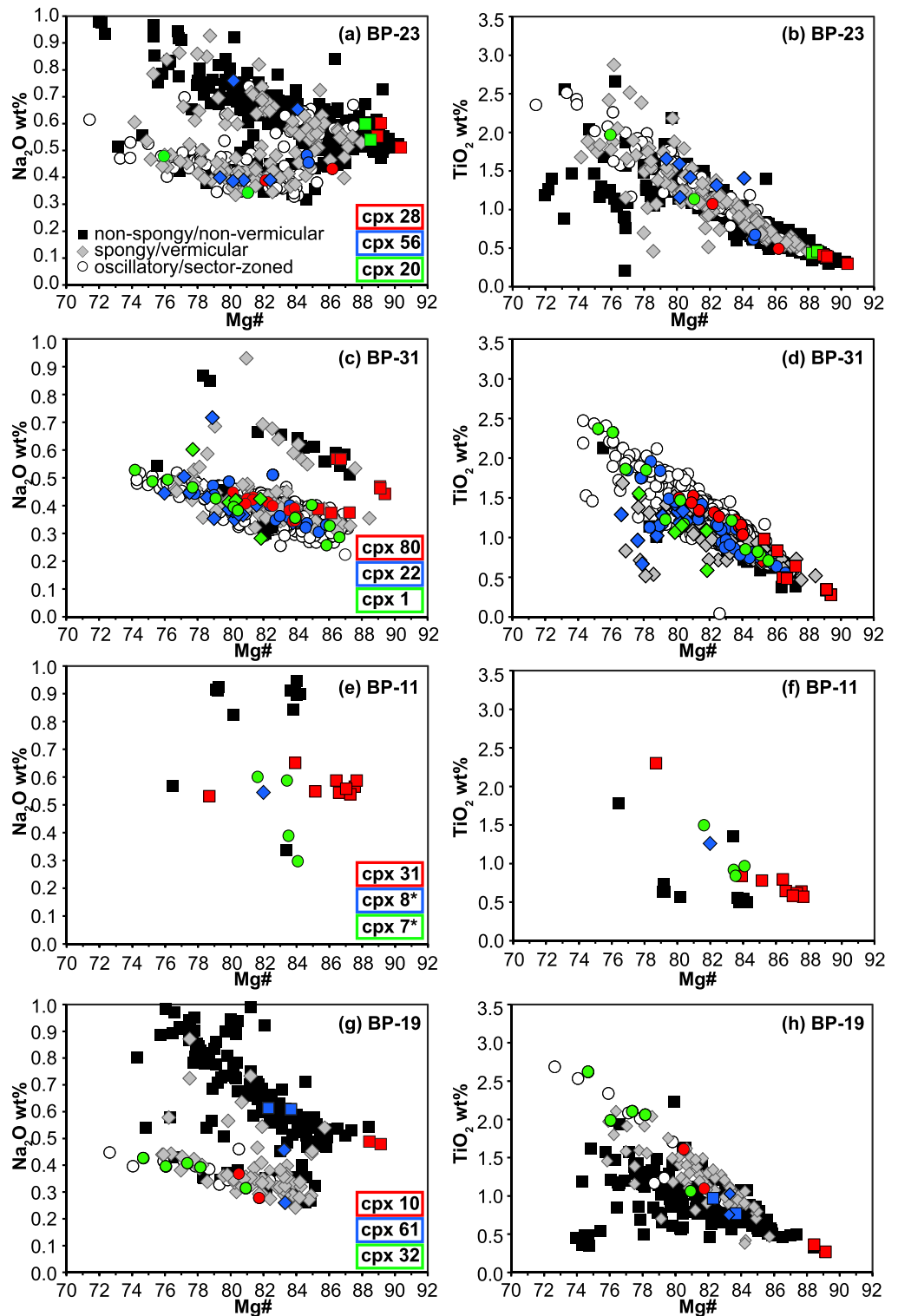
Figure 7. Plots of Na$_2$O wt% versus Mg# = (MgO/(MgO + FeO^T) × 100) (a, c, e, g) and TiO$_2$ wt% versus Mg# (b, d, f, h) in clinopyroxene crystals from four BPVF samples (BP-23, BP-31, BP-11, and BP-19). Additionally, three individual crystals are highlighted that collectively display examples of each textural category (one crystal can feature more than one texture). Individual analyses obtained across each crystal, with corresponding symbols that reflect the textural category for each analytical spot, are shown. Note that analyses from a single oscillatory- and sector-zoned crystal (cpx-1 in BP-31; Figure 8) span the entire compositional range as all zoned phenocrysts in this sample. Red crystals in each sample are the most Mg rich and used to constrain depth at which cpx began to crystallize.

non-spongy/non-vermicular   spongy/vermicular   oscillatory/sector zoned
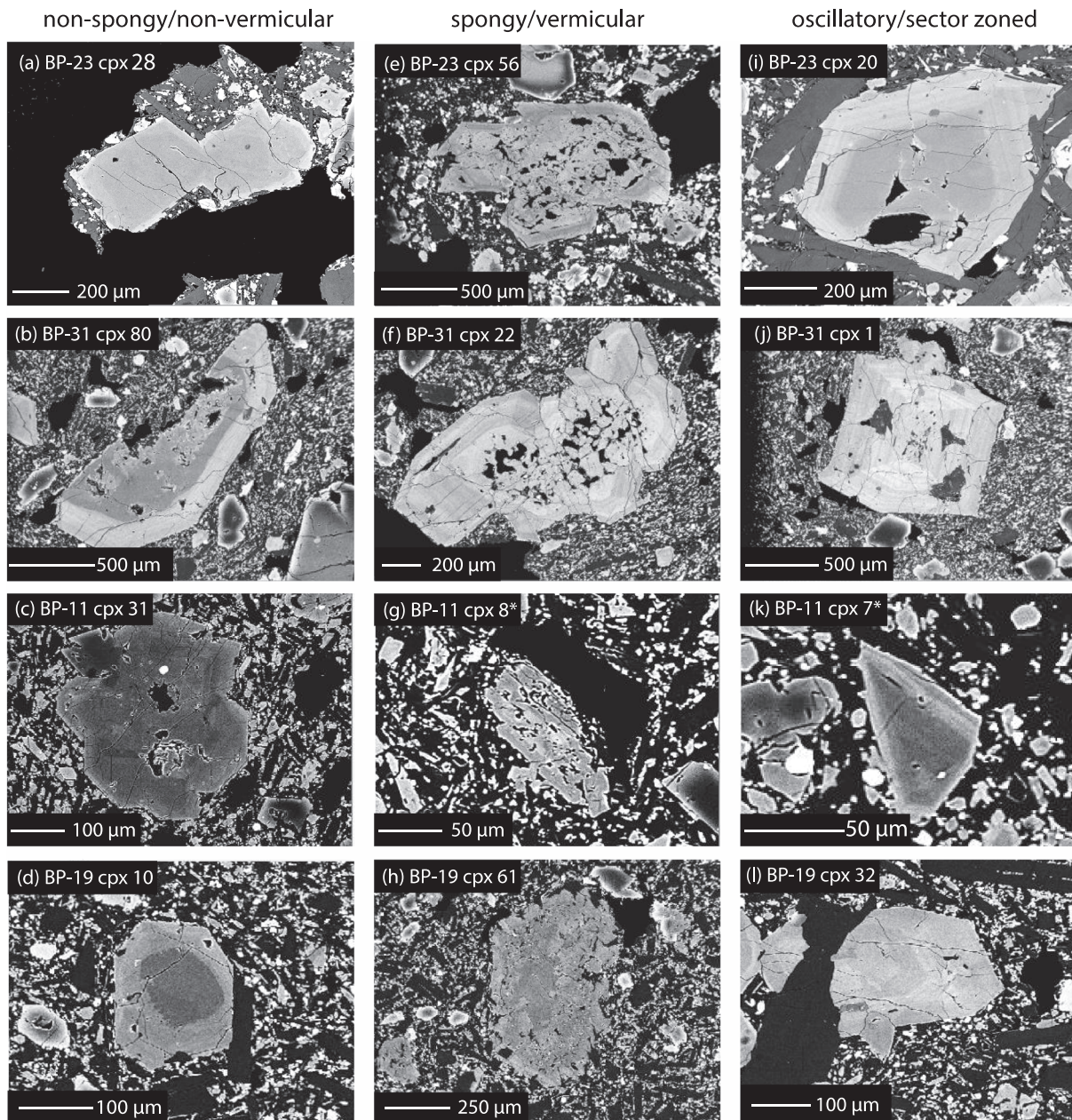
Figure 8. (a–l) Representative BSE images of clinopyroxene crystals from each texture category including nonspongy (nonvermicular, often as cores; panels a, b, d, i, and k), spongy (vermicular; as cores, panel f, and rims, panel h), and sector- and/or oscillatory-zoned crystals (sometimes rim only; panels b, d, f, i, and k). Two clinopyroxene crystals from BP-11 (cpx-7 and cpx-8) are microlites but are used here as examples of vermicular and sector- or oscillatory-zoned crystals. Individual analytical spots from these representative crystals are highlighted in Figure 7.

6. Evaluation of Phenocryst Growth During Ascent

6.1. Mantle Xenoliths in BP Basalts

The BP volcanic field provides an opportunity to test the hypothesis of phenocryst growth during ascent due to the presence of mantle xenoliths in some of the basalt flows (e.g., Beard & Glazner, 1995; Ducea & Saleeby, 1996; Lee et al., 2001; Wilshire et al., 1988). The most important observation is that in order for a mantle xenolith to be carried to the surface, the ascent velocity of the host basalt must be sufficiently rapid to overcome the settling velocity of the mantle xenolith. Calculated minimum ascent rates based on Stoke's settling law (see the supporting information for details on calculation), prior to the onset of phenocryst
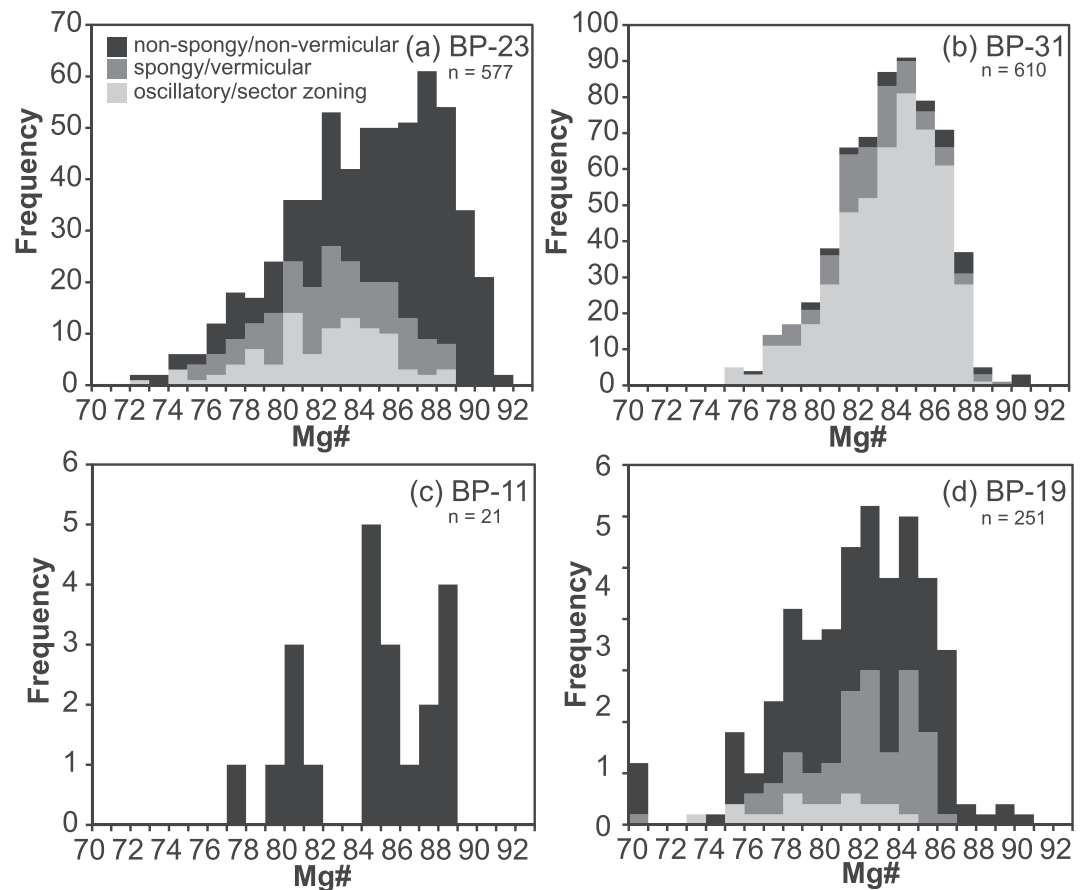
Figure 9. Histograms of Mg# in clinopyroxene crystals from four BP samples. Clinopyroxene analyses are given different colors according to texture to illustrate their relative abundance in each sample.

growth (e.g., Sparks et al., 1977; Spera, 1984), range from 6 to 24 km/day (dependent on whether dissolved water contents of 1.5 or 3.0 wt% are used to calculate melt viscosity). The results are consistent with the hypothesis that phenocryst growth in the BP basalts occurred rapidly during ascent (Figure 11), rather than slowly in a crustal magma chamber. To further test this hypothesis, the compositions and textures of olivine and clinopyroxene phenocrysts in the BP basalts are examined below.
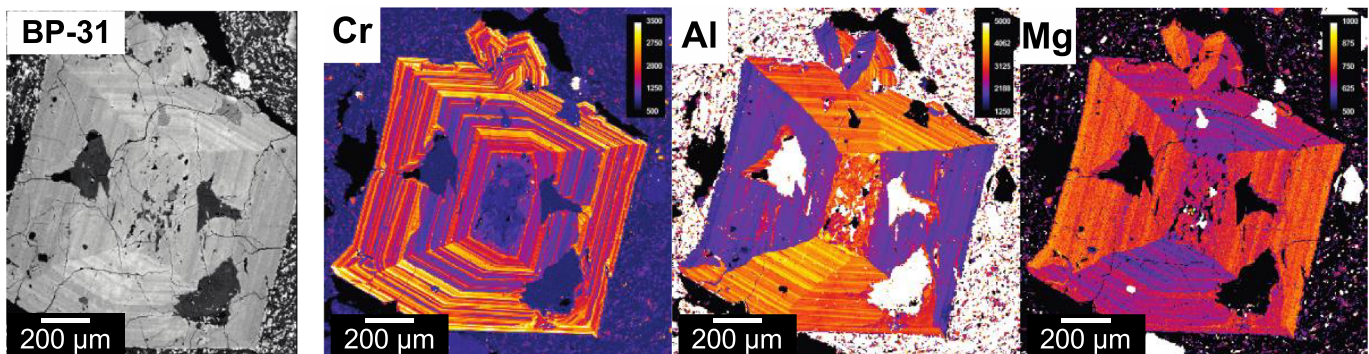
Figure 10. X-ray intensity maps of Mg, Cr, and Al in a representative clinopyroxene crystal from BP-31 (cpx-1 in Figures 7 and 8). Note that the compositional variation in this single crystal (Figures 7c and 7d) spans the entire range of all oscillatory and/or sector-zoned crystals in BP-31. Maps indicate that sector zoning strongly affects Al and Mg concentrations but not Cr contents. All three elements display oscillatory zoning.
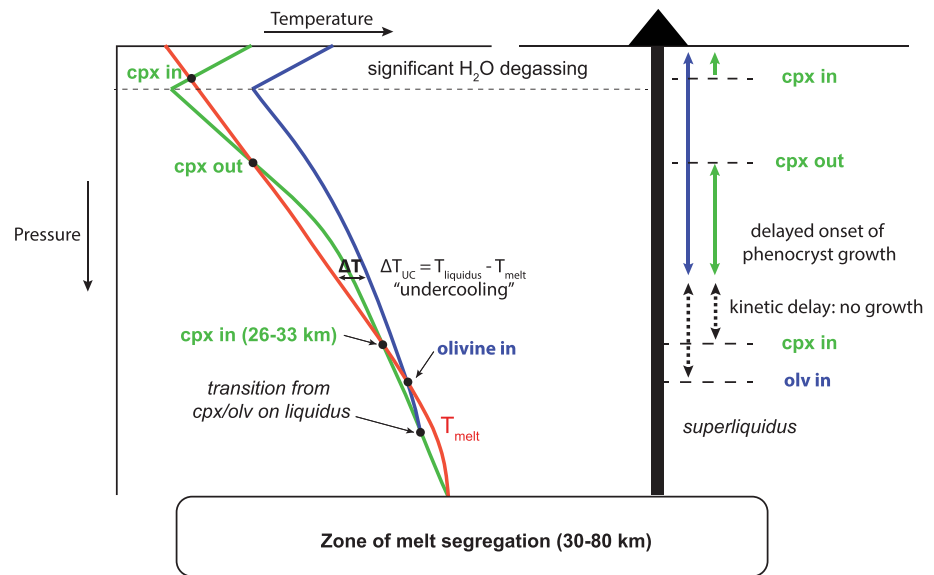
Figure 11. A schematic diagram that illustrates how melt temperature (red) and liquidus temperatures of olivine (blue) and clinopyroxene (green) may vary during ascent, leading to development of undercooling and rapid phenocryst growth. Each BP basalt is expected to segregate from its source region (~30–80 km depth; Putirka et al., 2012; Gazel et al., 2012) fluid undersaturated, which will cause its liquidus temperature to decrease during ascent. It is therefore plausible that initial ascent of basalt is superliquidus (i.e., the drop in melt temperature during initial ascent is smaller than the drop in liquidus temperature). Eventually, the ascending melt cools sufficiently to cross its liquidus, but from a superliquidus state, which leads to a kinetic delay in nucleation and crystal growth. This kinetic delay generates an undercooling ($\Delta T_{UC} = T_{liquidus} - T_{melt}$) and thus high crystal growth rates and low nucleation rates (e.g., Lofgren, 1974), leading to growth of large, sparse phenocrysts with diffusion-limited growth textures. The onset of clinopyroxene phenocryst growth occurs between 26 and 33 km, on the basis of clinopyroxene-melt barometry (Table 4).

6.2. Evidence of Diffusion-Limited Growth Textures in Phenocrysts From BPVF Basalts
6.2.1. Olivine

Many olivine phenocrysts in BP samples display melt diffusion-limited growth textures (e.g., hopper texture), as viewed in BSE images (Figure 6). Diffusion-limited growth textures are consistent with crystallization at an effective undercooling ($\Delta T_{UC} = T_{liquidus} - T_{melt}$) (e.g., Lofgren, 1974; Shea et al., 2019; Welsch et al., 2014). Undercooling may develop in basalts that lose little dissolved water from the melt during initial ascent (i.e., were fluid undersaturated at the time of melt segregation from their source or underwent open-system degassing of a CO_2-rich fluid phase). As illustrated in Figure 11, an ascending melt is expected to become superliquidus if its initial drop in temperature during ascent is less than that for the positive dP/dT slope of its fluid-undersaturated liquidus. During continued ascent and cooling, the melt will eventually cross its liquidus, but from a superliquidus condition (i.e., free of preexisting nuclei), which will lead to a kinetic delay in nucleation. This, in turn, allows an undercooling (ΔT_{UC}) to develop, where the melt (crystal free) is cooler than the liquidus. Moderate ΔT_{UC} values promote low nucleation rates and high crystal growth rates (e.g., Lofgren, 1974), conditions that promote initial dendritic and/or hopper growth of sparse phenocrysts. The complex P zoning observed in many of the BP olivine phenocrysts (Figure 5) has been interpreted as recording an initial period of rapid, diffusion-limited, dendritic growth (Milman-Barris et al., 2008; Shea et al., 2019; Welsch et al., 2012, 2014). The lack of P zoning in the San Carlos olivine (from mantle xenolith) is consistent with a different growth history that did not include rapid crystallization from an undercooled liquid.

6.2.2. Clinopyroxene

Among the three distinct types of textures displayed by the clinopyroxene phenocrysts in the BP basalts, two are indicative of diffusion-limited, rapid crystal growth. The vermicular (i.e., spongy) texture (Figures 8e–8h) may reflect an initial dendritic architecture that is then partially overgrown (Welsch et al., 2016). A similar texture is found in vermiform chromite crystals formed during rapid crystal growth experiments on basalts (Roeder et al., 2001). The sector-zoning texture, found in most of the low-Na_2O group of phenocrysts in the

BP basalts (Figures 7 and 8i–8l), also points to rapid crystal growth rates (e.g., Brophy et al., 1999; Shimizu, 1990; Ubide et al., 2019). Experimental studies (e.g., Kouchi et al., 1983; Skulski et al., 1994) show that sector zoning develops in clinopyroxene crystals at various undercooling ($\Delta T_{UC} = T_{liquidus} - T_{melt}$) conditions, leading to growth rates that vary with ΔT_{UC}. For example, Kouchi et al. (1983) report growth rates along the *010* sector that range from 1.6×10^{-7} cm/s (~138 μm/day) at ΔT_{UC} of 13°C to 7.5×10^{-6} cm/s (~6.5 mm/day) at ΔT of 45°C, consistent with growth of the clinopyroxene phenocrysts in BP basalts over a period of days. Skulski et al. (1994) grew phenocryst-sized (~220 μm) clinopyroxene crystals with sector zoning in a piston-cylinder run (1 GPa) within 24 hr.

The co-occurrence of oscillatory zonation (e.g., Cr, Al, and Mg) with sector zoning has been reported in several naturally occurring clinopyroxene phenocrysts, often in mafic melts (e.g., Brophy et al., 1999; Shimizu, 1990; Ubide et al., 2019). There is no broad consensus on the origin of the oscillatory zonation in clinopyroxene. Some studies point to magmatic recharge events (e.g., Ubide et al., 2019), whereas others conclude that kinetic effects at the crystal-melt interface play a dominant role (e.g., Shimizu, 1990), similar to the case presented for oscillatory zoning in plagioclase (e.g., Haase et al., 1980; L'Heureux, 1993). The X-ray intensity maps for the clinopyroxene phenocryst from BP-31 (Figure 10) clearly show that both types of zonation (sector and oscillatory) developed together, which broadly supports the role of various kinetic effects (consistent with rapid growth) in their respective development.

6.3. Evidence of Polybaric Phenocryst Growth of Clinopyroxene

In the high-Mg BP basalts, the occurrence of two distinct populations of clinopyroxene composition, reflected in plots of Na_2O versus Mg# (Figure 7), points to two distinct depth intervals for phenocryst growth. The high-Na_2O population points to an elevated jadeite component (Figure 7) and thus a greater pressure of crystallization for the nonspongy (nonvermicular) clinopyroxene. Mordick and Glazner (2006) also reported high-Na_2O contents (0.86–0.48 wt%) in several clinopyroxene crystals from the BP basalts and noted that they must have crystallized at relatively high pressures. In contrast, the oscillatory- and sector-zoned clinopyroxene, which often occurs as rims on clinopyroxene crystals, with a sharp compositional contrast between core and rim, is in the low-Na_2O group, which points to growth at low pressure. In some cases, the core appears to have a rounded (resorbed) shape adjacent to the oscillatory-zoned rims (Figures 8b, 8c, 8d, 8i, and 8k), which suggests an interval between the high-pressure and low-pressure growth of clinopyroxene, where clinopyroxene was not stable and resorption was not kinetically inhibited during ascent. Evidence of polybaric crystallization of clinopyroxene in a single basalt sample, and even in a single phenocryst within a sample, has been reported in recent studies (e.g., Hammer et al., 2016; Mollo et al., 2020).

In Figure 11, the schematic illustration depicts a viable hypothesis to explain the polybaric growth of clinopyroxene phenocrysts during ascent, consistent with available information of phase relations. For example, it is well known from phase-equilibrium experiments (e.g., Weaver et al., 2011) that the stability of clinopyroxene in basaltic melts is strongly dependent on pressure and that the temperature of the clinopyroxene-in curve decreases more strongly than that for olivine with decreasing pressure (e.g., MELTS; Asimow & Ghiorso, 1998; Ghiorso & Sack, 1995). It is therefore possible that there is a depth interval in the lower-middle crust, where the melt temperature is below the olivine- and clinopyroxene-in curves, but that in the middle-upper crust (prior to significant loss of H_2O from the melt due to degassing), the melt temperature may move above the clinopyroxene-in curve (Figure 11). This will be a depth interval that is marked by no clinopyroxene growth (and possibly some resorption). Then, as the melt continues to ascend into the upper crust, significant loss of H_2O will inevitably occur (due to degassing), causing the slope of the clinopyroxene-in (and olivine-in) curve to change sign. The melt temperature will cross the clinopyroxene-in curve again, leading to rapid growth of the oscillatory- and sector-zoned clinopyroxene under shallow, fluid-saturated conditions prior to eruption.

7. Evidence That the Most Mg-Rich Olivine Represents the Liquidus Phase in Each Sample

If phenocryst growth during ascent is a viable hypothesis for the BP basalts (Figure 11), it is possible that the most Mg-rich olivine observed in each sample (Figure 2) closely approximates the first phase to crystallize from a liquid with the composition of whole rock. In other words, if phenocryst growth was rapid, there
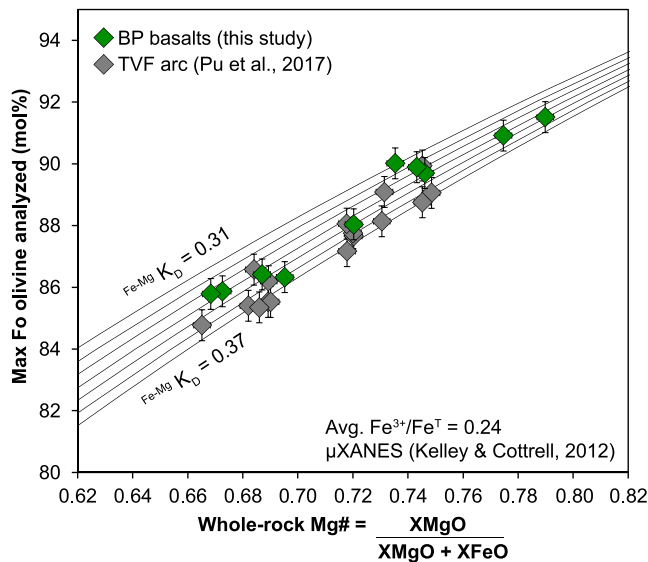
Figure 12. Plot of the most Mg-rich olivine analyzed in each BP sample versus the whole-rock Mg# (calculated with $Fe^{3+}/Fe^T = 0.24$, average of μ-XANES analyses; Kelley & Cottrell, 2012). Superimposed on this plot are isopleths of $^{Fe^{2+}-Mg}K_D$(olivine-melt). All BP samples from this study fall on K_D isopleths that range from 0.31–0.36 (expected values; Table 2) and thus pass the K_D liquidus test. Additionally, basalts (>5 wt% MgO) from the Mexican arc (TVF) from Pu et al. (2017) are shown for comparison, where whole-rock Mg# are also calculated using melt $Fe^{3+}/Fe^T = 0.24$. The most Mg-rich olivine in these basalts also pass the liquidus test, although none of the flows contain mantle xenoliths.

may not have been time for significant chemical reequilibration of the first (i.e., liquidus) olivine that initially grew from the melt. Thus, an evaluation of whether the most Mg-rich olivine analyzed in each sample has a composition expected for the liquidus olivine can be made.

To perform this assessment, hereafter referred to as the $^{Fe^{2+}-Mg}K_D$(olivine-melt) liquidus test, a plot of the most Mg-rich olivine phenocryst in each sample as a function of the whole-rock Mg# is shown in Figure 12. For the calculation of Mg#, it is assumed that the Fe^{3+}/Fe^T in each sample is 0.24 (average of μ-XANES analyses; Kelley & Cottrell, 2012). Superimposed on this plot are isopleths of $^{Fe^{2+}-Mg}K_D$(olivine-melt) values:

$$^{Fe^{2+}-Mg}K_D(olivine-melt) = \left(\frac{X_{Fe^{2+}O}}{X_{MgO}}\right)^{olivine}\left(\frac{X_{MgO}}{X_{Fe^{2+}O}}\right)^{melt} \quad (1)$$

The results show that the most Mg-rich olivine analyzed in the BP basalts overlap $^{Fe^{2+}-Mg}K_D$(olivine-melt) isopleths that range from 0.31 to 0.36 (Table 2), which broadly match the range of values calculated from various models in the literature (0.32–0.36; Table 3), including the MELTS thermodynamic model (Asimow & Ghiorso, 1998; Ghiorso & Sack, 1995) and the Putirka (2016) model. The K_D values from MELTS do not vary with oxidation state between ΔQFM = −1 to +1, and the value at ΔNNO = 0 is reported in Table 2. For the Putirka (2016) model, the effect of pressure on the K_D value is negligible at crustal depths. Pu et al. (2017) showed that ~5–6 wt% dissolved H_2O leads to an increase in $^{Fe^{2+}-Mg}K_D$(olivine-melt) value by ≤0.03, and thus, a small increase in K_D of ~0.01 is possible for the BP basalts and is also evaluated (Table 3).

The results in Figure 12 and Table 2 strongly support the hypothesis that the most Mg-rich olivine analyzed in each sample closely represents the first olivine to crystallize from a liquid with the whole-rock composition (i.e., pass the $^{Fe^{2+}-Mg}K_D$(olivine-melt) liquidus test), which is consistent with phenocryst growth of olivine during ascent (Figure 11). Also shown in Figure 12 are data from Pu et al. (2017) for 16 basaltic samples (>5 wt% MgO) from the Mexican arc (TVF). Collectively, the results for both volcanic fields show that phenocryst growth during ascent and preservation of the first olivine composition to crystallize from the melt is not uncommon, even in samples without mantle xenoliths.

7.1. Consistency With Fe-Ti Two-Oxide Oxybarometry and Whole-Rock FeO Analyses

The approach taken in Figure 12 can be inverted to extract information on the melt Fe^{3+}/Fe^T ratio at the onset of olivine crystallization for each of the BP samples, using $^{Fe^{2+}-Mg}K_D$(olivine-melt) values calculated for each sample from MELTS (Asimow & Ghiorso, 1998; Ghiorso & Sack, 1995) and Putirka (2016) (Table 3). The results can then be compared to the Fe-Ti two-oxide oxybarometry results for BP-20 (Table S7). Through application of Equation 1, the only unknown in this calculation is the concentration of ferrous iron in the liquid (X_{FeO}^{liq}). Resulting Fe^{3+}/Fe^T ratios are shown as histograms in Figure 13. Additional histograms illustrating the effect of an increase in $^{Fe^{2+}-Mg}K_D$(olivine-melt) values of +0.01 applied to those from MELTS and Putirka (2016) due to the effect of ~1.5 wt% dissolved H_2O (Gazel et al., 2012) are shown for comparison (Figures 13b and 13d).

Among the four histograms (Figure 13), the average (±1σ) Fe^{3+}/Fe^T ratios range from 0.25 (±0.04) to 0.22 (±0.03), which overlap the average Fe^{3+}/Fe^T ratio (0.24 ± 0.01) from μ-XANES (Kelley & Cottrell, 2012). Importantly, among the four samples with the lowest calculated Fe^{3+}/Fe^T ratios (in all four histograms; Figure 13), ilmenite was found in three of them, which is consistent with the stabilization of ilmenite at slightly lower fO_2 conditions compared to rest of the BP samples. For Sample BP-20, the onset of two-oxide crystallization occurred at ΔNNO = −0.45 ($Fe^{3+}/Fe^T = 0.19$) and thus overlaps the calculated Fe^{3+}/Fe^T values for the ilmenite-bearing samples on the basis of olivine-melt oxybarometry. Because the average

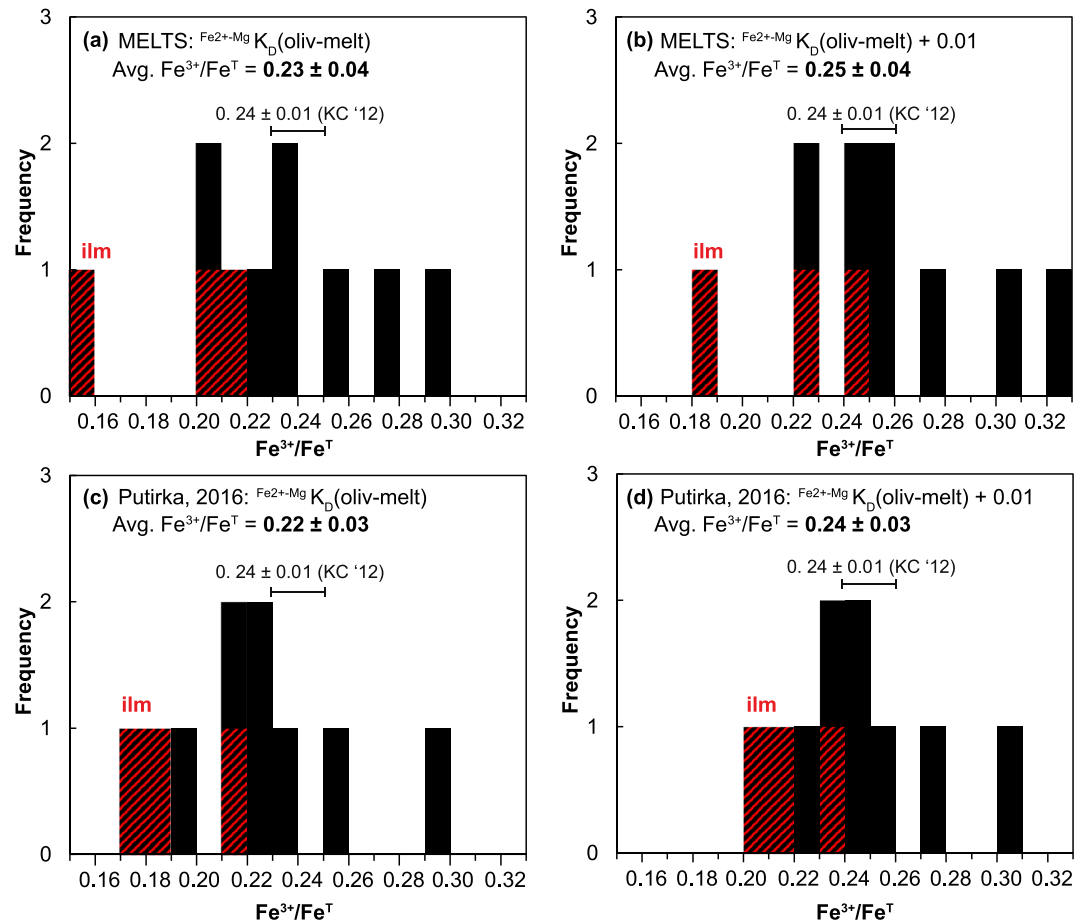**Figure 13.** Histograms of melt Fe^{3+}/Fe^T values calculated using the most Mg-rich olivine analyzed in each sample, the whole-rock composition, and an $^{Fe^{2+}-Mg}K_D$(olivine-melt) value for that basalt liquid. Panels (a) and (c) demonstrate variation in calculated melt Fe^{3+}/Fe^T ratios when using $^{Fe^{2+}-Mg}K_D$(olivine-melt) values calculated from MELTS (ΔNNO = 0, anhydrous, Asimow & Ghiorso, 1998; Ghiorso & Sack, 1995) and the model of Putirka (2016), respectively. Panels (b) and (d) illustrate the effect of an increase in melt $^{Fe^{2+}-Mg}K_D$(olivine-melt) values of +0.01 applied to those from MELTS and Putirka (2016) due to the effect of dissolved melt H_2O (1.5 wt%, Gazel et al., 2012). Most Fe^{3+}/Fe^T values overlap the average analyzed value by μ-XANES in olivine-hosted melt inclusions (0.24 ± 0.01; Kelley & Cottrell, 2012). In all four histograms, three of the four lowest melt Fe^{3+}/Fe^T ratios are in samples that contain ilmenite.

Fe^{3+}/Fe^T ratio in all four histograms do not vary significantly from one another, the effect of using different models to calculate the K_D value, and adding 0.01 to reflect the effect of >1.5 wt% H_2O (Gazel et al., 2012; Pu et al., 2017) has little impact. The results in Figure 13 provide evidence that the most Mg-rich olivine in each BP sample passes the $^{Fe^{2+}-Mg}K_D$(olivine-melt) liquidus test.

An additional test of whether the most Mg-rich olivine is the liquidus composition is obtained by comparing the ferrous iron concentration in each sample calculated from olivine-melt oxybarometry (Equation 1) with those directly measured in the whole-rock sample by the Wilson (1960) titration method. In Figure 14, four 1:1 plots of wt% FeO are shown based on the four different sets of $^{Fe^{2+}-Mg}K_D$ (olivine-melt) values presented in Figure 13. Also shown are results from Crabtree and Lange (2012) and Waters and Lange (2016) on andesite, dacite, and rhyolite samples, where Fe-Ti oxide oxybarometry, instead of olivine-melt oxybarometry (Equation 1), was used to constrain preeruptive wt% FeO concentrations. Samples BP-11 and BP-16, with evidence of alteration and heterogeneity, are shown as open symbols. The error bars reflect ±2σ analytical uncertainties in the titration results for each sample, and the propagated error in the FeO concentration (±0.29 − 0.41 wt%) from olivine-melt oxybarometer was derived from an uncertainty of ±0.02 in the $^{Fe^{2+}-Mg}K_D$(olivine-melt) value. The results show a close adherence to the 1:1 line in all four plots.
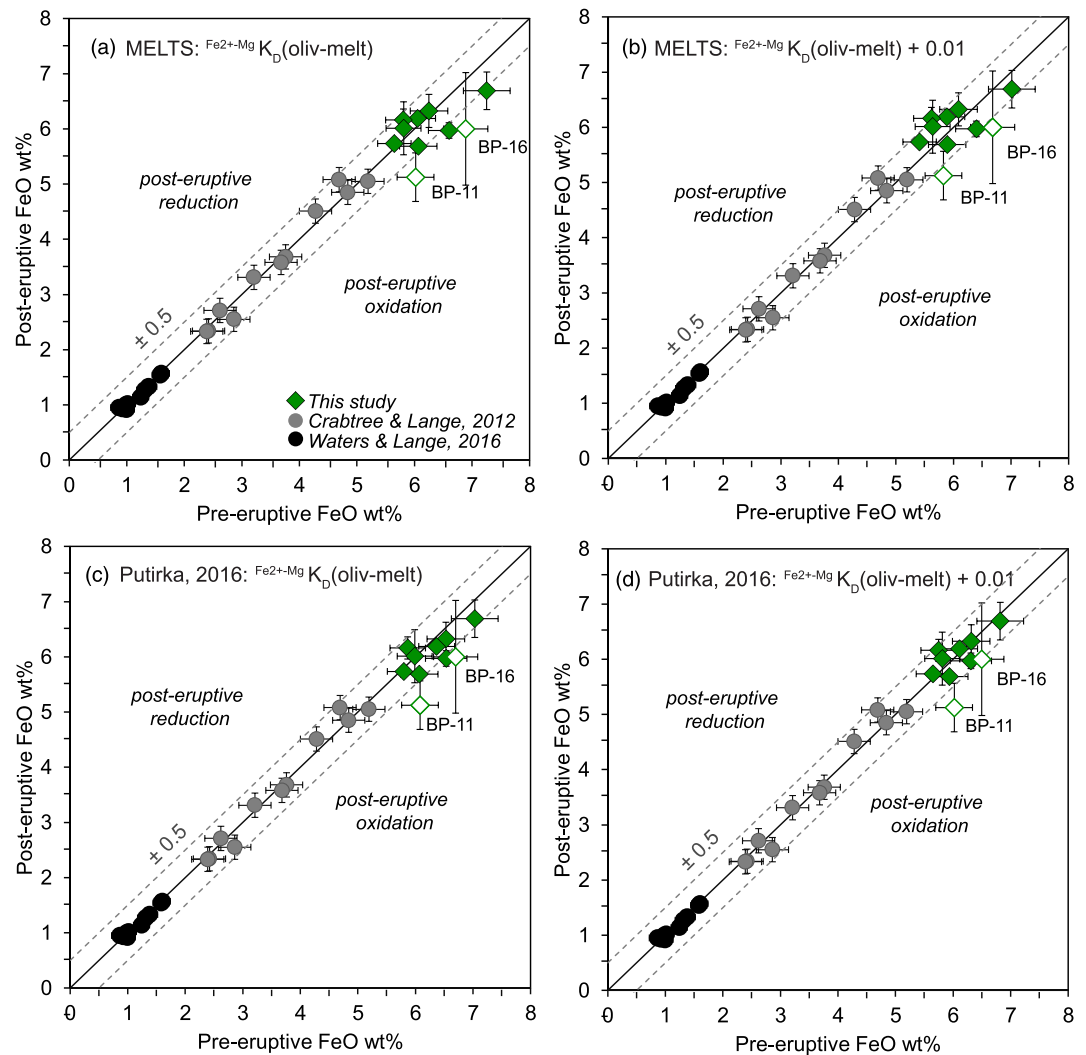
Figure 14. Four 1:1 plots of posteruptive wt% FeO analyzed by the Wilson (1960) titration method versus preeruptive wt% FeO obtained using olivine-melt oxybarometry at the liquidus, with the four $^{Fe^{2+}-Mg}K_D$(olivine-melt) values presented in Figure 13. Results from this study on BP basalts are compared to those from Crabtree and Lange (2012) and Waters and Lange (2016) on andesite, dacite, and rhyolite samples, where Fe-Ti oxide oxybarometry was used, instead of olivine-melt oxybarometry. Samples BP-11 and BP-16, with posteruptive alteration products in its vesicles or heterogeneity between measurements, are shown with open symbols. The 1:1 line is shown with dashed lines at ± 0.5 wt% FeO.

8. Olivine-Melt Thermometry

The collective data in Figures 12–14 confirm that the most Mg-rich olivine in each sample closely represents the first olivine to crystallize from the whole-rock liquid composition. This enables thermometry to be applied to this olivine-melt pairing in order to calculate temperature at the onset of phenocryst growth in each sample.

Numerous olivine-melt thermometers based on the partitioning of Mg ($D_{Mg}^{ol/liq}$) have been presented in the literature. In a review of these thermometers, Putirka (2008) showed that the Beattie (1993) form of the Mg-based thermometer is the best at recovering experimental temperature under anhydrous conditions and produces temperatures similar to those obtained by the MELTS thermodynamic model (Asimow & Ghiorso, 1998; Ghiorso & Sack, 1995). However, one of the limitations of this thermometer is that $D_{Mg}^{ol/liq}$ is strongly sensitive to dissolved water in the melt (e.g., Almeev et al., 2007; Médard & Grove, 2008), which leads to calculated temperatures that are too high if not corrected for the effect of H_2O. To address this problem, Putirka et al. (2007) calibrated an olivine-melt thermometer based on $D_{Mg}^{ol/liq}$ that
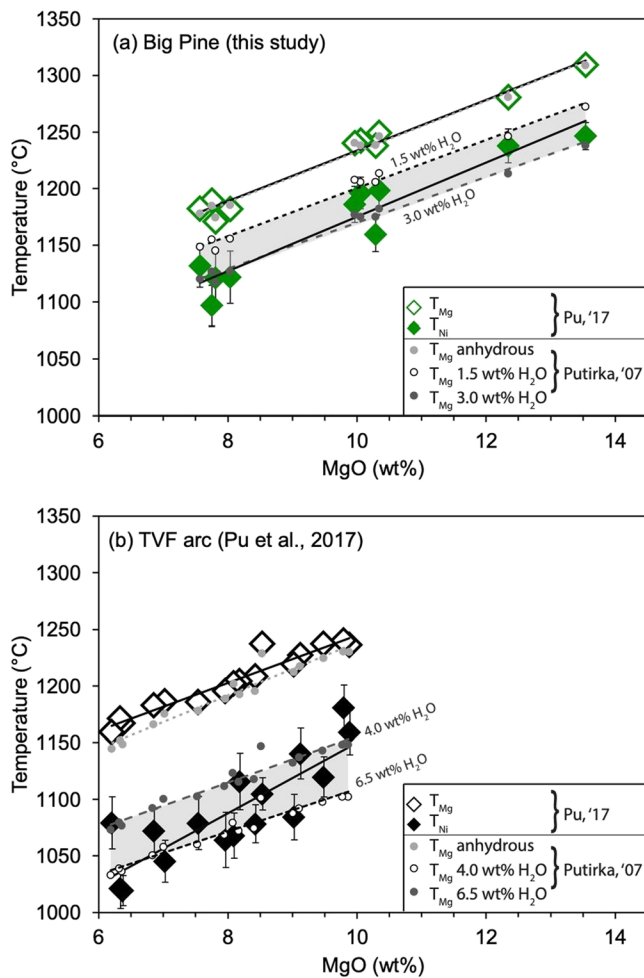
Figure 15. Calculated temperatures (°C) from olivine-melt Mg and Ni thermometers (T_{Mg} and T_{Ni}, respectively) from Pu et al. (2017) versus whole-rock MgO (wt%) for (a) BP basalts and (b) Mexican arc basalts (TVF, Pu et al., 2017). Temperature error bars (Table 2) are from propagated analytical uncertainty and are within the symbol size for T_{Mg}. The average ΔT ($=T_{Mg} - T_{Ni}$) is approximately 59°C for the BP basalts and 115°C for the TVF arc basalts. Temperatures from the H_2O-corrected Mg thermometer of Putirka et al. (2007) are shown for comparison. For the BP basalts, those corrected for 1.5 and 3.0 wt% H_2O (analyses from Gazel et al., 2012) overlap Ni temperatures (which require no H_2O correction; Pu et al., 2017). For the TVF arc basalts, temperatures corrected for 4.0–6.0 wt% H_2O (consistent with olivine-hosted melt inclusion analyses from Johnson et al., 2008, 2009) overlap calculated T_{Ni} values.

includes a correction for H_2O in the melt. Its application requires that water contents in the melt be known, which can be obtained from volatile analyses of olivine-hosted melt inclusions (e.g., Gazel et al., 2012).

Because information on melt water contents is not always known for all basalt samples, Pu et al. (2017) developed an olivine-melt thermometer based on the partitioning of Ni ($D_{Ni}^{ol/liq}$), which shows no dependence on dissolved water in the melt or pressure under crustal (<1 GPa) conditions (Pu, 2018). Thus, the Ni thermometer provides the actual temperature at the onset of olivine growth, because it requires no correction for H_2O content. In the Pu et al. (2017) study, two olivine-melt thermometers (based on $D_{Mg}^{ol/liq}$ and $D_{Ni}^{ol/liq}$) were calibrated on the same set of one hundred twenty-three 1 bar experiments (4–40 wt% MgO), and the resulting models recover the experimental temperatures equally well. The average ($\pm 1\sigma$) temperature difference between the two thermometers (i.e., $T_{Mg} - T_{Ni}$) is 1 (± 29)°C. Therefore, any systematic difference in calculated temperatures between the two thermometers, when applied to the same basalt, cannot be attributed to differences in their respective calibrations but instead may reflect the role of dissolved H_2O in the melt.

In this study, the Mg- and Ni-based olivine-melt thermometers from Pu et al. (2017) were applied to all BP samples in Table 1. For the Mg thermometer, values of $D_{Mg}^{ol/liq}$ were constructed from the most Mg-rich olivine in each sample paired with a liquid of its whole-rock composition and are reported in Table 2. Resulting temperatures from the Mg thermometer (T_{Mg}) range from 1309–1170°C for melts that range from 13–7 wt% MgO (Table 2 and Figure 15). Analytical uncertainties in $D_{Mg}^{ol/liq}$, derived from the microprobe and whole-rock analytical errors, are relatively low (0.9–1.5%) and lead to propagated uncertainties in T_{Mg} of ± 4–5°C. For the Ni thermometer, values of $D_{Ni}^{ol/liq}$ were constructed for the most Mg-rich olivine in each sample based on a linear fit to the olivine data (wt% NiO vs. mol% Fo content) in Figure 3. This linear fit reduces the analytical scatter in the NiO wt% data due to microprobe error and provides a more accurate estimate of the NiO wt% in the most Mg-rich olivine in each sample. Resulting temperatures (T_{Ni}) range from 1247–1097°C and are systematically lower than those obtained with the Mg thermometer (Table 2 and Figure 15a). Analytical uncertainties in $D_{Ni}^{ol/liq}$, derived from errors in the olivine (± 0.02 wt% NiO) and the whole-rock (± 4 ppm Ni) compositions, range from 5–11% and lead to propagated uncertainties in T_{Ni} of ± 12–23°C. Pu et al. (2017) note that additional error exists if the most Mg-rich olivine crystal is not used (e.g., not exposed/analyzed or lost to diffusive reequilibration). Therefore the most Mg-rich olivine composition is considered a minimum value. Calculated temperatures using both the Mg and Ni thermometers are thus maximum values, and
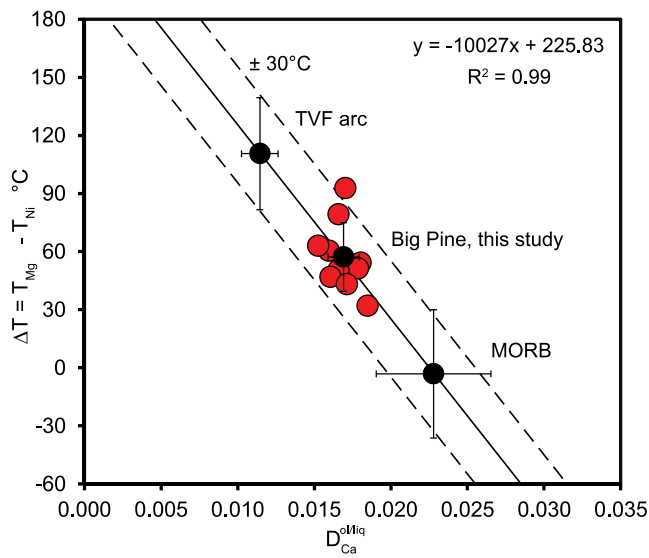
ΔT ($=T_{Mg} - T_{Ni}$) is a minimum estimate. Pu et al. (2017) calculate that a decrease in Fo by 1 mol% results in ΔT values that are 13–46°C too low for their samples. Again, because $D_{Ni}^{ol/liq}$ is insensitive to dissolved water and variations in crustal pressure (Pu, 2018), T_{Ni} values give the actual temperature at the onset of olivine growth.

9. Olivine-Melt Hygrometry

The thermometry results in Figure 15a show that temperatures based on $D_{Mg}^{ol/liq}$ (T_{Mg}) are systematically higher than those based on $D_{Ni}^{ol/liq}$ (T_{Ni}), and both systematically decrease with decreasing MgO content in the melt. The average temperature difference between the two thermometers ($T_{Mg} - T_{Ni}$) is ~59°C (Figure 15a), which points to the presence of dissolved water in the BP basalts. Similar differences in

Figure 16. Average ΔT ($=T_{Mg} - T_{Ni}$) versus molar $D_{Ca}^{ol/liq}$ for basalts from three distinct volcanic fields (tectonic settings), including (1) Mexican arc basalts (TVF; Pu et al., 2017), (2) mid-ocean ridge basalts (Allan et al., 1989; Pu et al., 2017), and (3) BP basalts from this study. A linear fit through the average of all three basalt groups shows a strong inverse correlation ($R^2 = 0.99$; $y = -10,027x + 225.83$). Larger ΔT (and thus higher melt H_2O, due to its suppression of olivine liquidus; see text) correlates negatively with mol% D_{Ca}, where lower values are associated with higher melt water contents (e.g., Gavrilenko et al., 2016). Note that results for individual BP basalts (red) plot along the trend line within the $\pm 30°C$ dashed error bars.

temperature ($T_{Mg} - T_{Ni}$) were obtained by Pu et al. (2017) on a suite of Mexican arc basalts (Figure 15b), where both the Mg and Ni thermometers were applied. In that study, the average ΔT ($=T_{Mg} - T_{Ni}$) value was 114°C, which is nearly twice as large as the average value of 59°C from this study (Figure 15). Since values of ΔT ($=T_{Mg} - T_{Ni}$) reflect the depression of the olivine liquidus due to dissolved water in the melt, the expectation is that the Mexican arc basalts were more hydrous than the BP basalts. This prediction is consistent with water analyses in olivine-hosted melt inclusions, with 3.9–5.7 wt% in the Mexican basalts (Johnson et al., 2008, 2009) and 1.5–3.0 wt% in the BP basalts (Gazel et al., 2012). The average ΔT values of ~114°C and ~59°C can be converted into an average estimate of melt water content of ~3.8 and 1.7 wt%, respectively, for the Mexican and BP basalts using the model of Médard and Grove (2008).

Another assessment of melt water contents can be made through application of the Putirka et al. (2007) Mg-based olivine-melt thermometer, which includes a correction for dissolved water content. In the absence of any H_2O correction, application of the Putirka thermometer to the BP basalts leads to calculated temperatures that closely match those obtained by the Pu et al. (2017) Mg thermometer (Table 2 and Figure 15). The next step is to input the water contents (1.5–3.0 wt%) from Gazel et al. (2012) into the H_2O-corrected Mg thermometer of Putirka et al. (2007; Equation 4) and calculate temperatures for all BP samples. A comparison of these H_2O-corrected temperatures to those obtained with the Ni thermometer of Pu et al. (2017) shows excellent agreement (Figure 15). The results illustrate that the Ni thermometer of Pu et al. (2017) matches the results for the H_2O-corrected thermometer of Putirka et al. (2007) when the water contents from Gazel et al. (2012) are employed. Note also that under anhydrous conditions, when the respective Mg thermometer of Putirka et al. (2007) and Pu et al. (2017) is each applied to all 10 BP basalts, the deviations in temperature are ≤4°C (Table 2 and Figure 15a).

A similar assessment can be made on the 16 basalts (>5 wt%) from the Mexican arc from Pu et al. (2017), where the Putirka et al. (2007) H_2O-corrected Mg thermometer is applied (Figure 15b.) When a range of melt H_2O content (4.0–6.5 wt%) consistent with measured values in olivine-hosted melt inclusions (3.9–5.7 wt%; Johnson et al., 2008, 2009) is applied, temperatures show agreement with those from the Ni thermometer (Pu et al., 2017; Figure 15b). Melt H_2O contents measured in melt inclusions are minimum estimates, and a slightly higher melt H_2O content is needed to capture the range of calculated T_{Ni} values. This result shows that phenocryst growth during ascent may be common and that olivine-melt thermometry/hygrometry can be applied at the liquidus in basalts that do not contain mantle xenoliths.

In summary, the internal consistency among four independent studies (Gazel et al., 2012; Médard & Grove, 2008; Pu et al., 2017; Putirka et al., 2007) lends credibility not only to the various thermometers that are employed in Figure 15 but also to the hypothesis that the T_{Ni} temperatures are those at the onset of olivine crystallization during ascent of the basalt samples. In other words, the pairing of the most Mg-rich olivine analyzed in each sample with the whole-rock composition of each sample is a valid approach.

9.1. Correlation Between $D_{Ca}^{ol/liq}$ and Depression of Olivine Liquidus Due to H_2O

Additional verification of the hydrous nature of the BP basalts is seen with an examination of the partition coefficient for $D_{Ca}^{ol/liq}$ using the most Mg-rich olivine paired with the whole-rock composition (proxy for liquid at onset of olivine crystallization). It has been proposed in the literature (e.g., Gavrilenko et al., 2016) that $D_{Ca}^{ol/liq}$ values are a function of dissolved water content, with a potential to be used as an olivine-melt hygrometer. Here, a comparison is made between the average ΔT ($=T_{Mg} - T_{Ni}$) values, obtained from the Pu et al. (2017) thermometers, and the average $D_{Ca}^{ol/liq}$ values obtained for three sets of basalts: (1) the BP basalts from this study, (2) Mexican arc basalts (Pu et al., 2017), and (3) the suite of mid-ocean ridge basalts (Allan et al., 1989) examined in Pu et al. (2017). The data are plotted in Figure 16 and reveal a strong inverse,

linear correlation ($R^2 = 0.99$) among the averages from each volcanic field. The highest $D_{Ca}^{ol/liq}$ values correspond to the mid-ocean ridge basalts from Allan et al. (1989), which are nearly anhydrous (~0.1 wt% H_2O), whereas those samples with the lowest $D_{Ca}^{ol/liq}$ values correspond to the Mexican arc basalts, which have the highest analyzed water contents (≤ 5.7 wt% H_2O; Johnson et al., 2009). As expected, the BP basalts have $D_{Ca}^{ol/liq}$ values in between those for the MORBs and arc basalts, consistent with melt water contents higher than those for mid-ocean ridge basalts, yet lower than those for active arc basalts. Thus, the $D_{Ca}^{ol/liq}$ values in Figure 16 provide independent corroboration that the application of both the Mg and Ni thermometers from Pu et al. (2017) to basalts (with olivine compositions that pass the $^{Fe^{2+}-Mg}K_D$ liquidus test) provides accurate constraints on temperature and melt water contents at the onset of olivine crystallization.

9.2. Minimum Water Contents at Onset of Plagioclase Phenocryst Growth

A final evaluation of dissolved water contents in the melt can be made by applying the plagioclase-liquid hygrometer (Waters & Lange, 2015) to the four samples that contain plagioclase phenocrysts. This approach only constrains minimum melt water contents since the temperature and melt composition at the onset of plagioclase crystallization are not known, only those at the onset of olivine growth at the liquidus. Nonetheless, because using a temperature that is too high and a melt composition that is too mafic both lead to melt water contents that are systematically too low, minimum water contents can be obtained. Therefore, a pairing of the most An-rich plagioclase to the whole-rock (liquid) composition at T_{Ni} was performed for each sample. The results are illustrated in Figure S4 and lead to minimum H_2O contents of 1.5, 1.6, 1.4, and 0.9 wt%, respectively, for BP-16, BP-30, BP-8 and BP-20, which are fully consistent with the melt inclusion analyses of Gazel et al. (2012).

10. Pressure (Depth) at Onset of Clinopyroxene Growth

Five of the BP samples (those with highest MgO content) contain clinopyroxene phenocrysts. In each of these five samples, when the most Mg-rich clinopyroxene composition (consistently from the nonspongy group; Tables 3 and 4) is paired with the whole-rock composition, the resulting $^{Fe^T-Mg}K_D$ (cpx-melt) value (using total iron; FeO^T) ranges from 0.26–0.31 (Table 4). These $^{Fe^T-Mg}K_D$ values overlap the range expected for clinopyroxene-liquid equilibrium (0.27 ± 0.03; Putirka, 2008), which shows that both clinopyroxene and olivine were closely cosaturated at the onset of phenocryst growth.

The Neave and Putirka (2017) clinopyroxene-liquid barometer was applied to the most Mg-rich clinopyroxene paired with the whole-rock liquid composition for each sample. This geobarometer is dependent on temperature, and therefore, the Ni-based temperature (T_{Ni}; Table 2) at the onset of phenocryst growth was used. The results give the pressure at the onset of clinopyroxene growth in these five samples, namely, 0.73, 0.73, 0.89, 0.77, and 0.69 GPa for BP-23, BP-31, BP-11, BP-19, and BP-24, respectively (Tables 3 and 4). Note that the use of lower temperatures (below liquidus values) and more evolved melt compositions (more differentiated than the whole-rock composition) both lead to shallower calculated pressures, and therefore, the pressures in Tables 3 and 4 are maximum values. Thus, the trend of increasing Na_2O with decreasing Mg# (among the high-Na_2O, nonspongy group; Figure 7) does not preclude phenocryst growth during ascent. In other words, the effect of lower melt temperature and more evolved melt composition (due to progressive crystallization of olivine and clinopyroxene) will lead to higher Na_2O contents in clinopyroxene during crustal ascent.

11. Implications and Conclusions

There are several key conclusions that can be drawn from this study. First and foremost, there is abundant evidence to support the hypothesis that phenocryst growth of olivine (and clinopyroxene) in the BP basalts occurred rapidly during ascent along fractures. Lines of evidence include the presence of mantle xenoliths in several flows, diffusion-limited growth textures in olivine and clinopyroxene, and polybaric crystallization of clinopyroxene phenocrysts.

Second, when the most Mg-rich olivine analyzed in each BP basalt is paired with a liquid composition that matches that for the whole rock, and a melt Fe^{3+}/Fe^T ratio of 0.24 (average from μ-XANES analyses; Kelley & Cottrell, 2012) is used, the resulting $^{Fe^{2+}-Mg}K_D$(olivine-melt) values match those predicted from various K_D

models from literature. In other words, the most Mg-rich olivine in each sample passes the $^{Fe^{2+}-Mg}K_D$(olivine-melt) liquidus test. This observation points to rapid ascent of the host basalt such that there was insufficient time for reequilibration of the first olivine composition to crystallize from the melt. For those basalts that also contain clinopyroxene phenocrysts, the most Mg-rich clinopyroxene also passes the $^{Fe^T-Mg}K_D$ (cpx-melt) liquidus test, suggesting that the two phases were closely cosaturated at the onset of phenocryst growth in five of the high-MgO BP basalts.

The third major conclusion is that olivine-melt thermometry and hygrometry can be applied to the most Mg-rich olivine in each sample paired with a liquid composition that matches the whole rock, for pairs that pass the $^{Fe^{2+}-Mg}K_D$(olivine-melt) liquidus test. Calculated temperatures based on $D_{Ni}^{ol/liq}$ (Pu et al., 2017), which is independent of dissolved water in the melt (Pu, 2018), are ~60°C lower, on average, than those based on $D_{Mg}^{ol/liq}$, which gives the temperature under anhydrous conditions (T_{Mg}). According to the Médard and Grove (2008) model, a depression of the olivine liquidus by ~60°C is expected for a melt water content of ~1.7 wt% H_2O, which matches the H_2O contents directly measured in olivine-hosted melt inclusions (~1.5–3.0 wt%; Gazel et al., 2012). The accuracy of the temperatures based on the Ni thermometer (T_{Ni}), which range from 1273–1097°C, is further confirmed by application of the H_2O-corrected Mg thermometer of Putirka et al. (2007) using the H_2O contents analyzed by Gazel et al. (2012). Finally, values of $D_{Ca}^{ol/liq}$ scale linearly and inversely with the magnitude of the depression of the olivine liquidus ($\Delta T = T_{Mg} - T_{Ni}$) due to dissolved water in the melt, which confirms previous work in the literature indicating that $D_{Ca}^{ol/liq}$ has the potential to be used as an olivine-melt hygrometer (Gavrilenko et al., 2016).

A fourth conclusion is that the depth for the onset of phenocryst growth can be estimated for the five basalts that were cosaturated with olivine and clinopyroxene at the onset of phenocryst growth. When the olivine-liquidus temperatures are used to calculate pressure with the clinopyroxene-melt barometer of Neave and Putirka (2017), results for the onset of phenocryst growth range from 0.7–0.9 GPa.

The overall results from this study show that the hypothesis of rapid growth of olivine (and clinopyroxene) phenocrysts during ascent and whether the most Mg-rich olivine analyzed in each sample represents the first phenocryst to grow at the liquidus can both be tested in individual basalt samples. This approach is best applied to samples where olivine is either the liquidus or near-liquidus phase and thus is likely best applied to samples ≥5 wt% MgO. To perform the $^{Fe^{2+}-Mg}K_D$(olivine-melt) liquidus test, a large set of microprobe analyses of numerous olivine crystals in each sample is required and an estimate of melt ferric-ferrous ratio is needed (from V-partitioning between olivine-melt, μ-XANES analyses of olivine-hosted melt inclusions, Fe-Ti oxide oxybarometry, and/or whole-rock FeO analyses of fresh, unaltered samples). For those samples where the pairing of the most Mg-rich olivine composition with the whole-rock composition passes the $^{Fe^{2+}-Mg}K_D$(olivine-melt) liquidus test, application of olivine-melt thermometry and hygrometry can be applied at the liquidus, leading to key constraints on the temperature and melt water content at the onset of phenocryst growth. Because this approach only requires microprobe analyses of olivine analyses in thin sections (and whole-rock major-element and Ni contents), it can readily be applied to obtain large global data sets. To date, this approach has been verified for basalts from the BP volcanic field (this study) and the Tancítaro volcanic field in the Mexican arc (Pu et al., 2017). The ready attainment of large global data sets will allow the question of whether there are distinctly different temperatures and water contents in basalts erupted within and between different tectonic settings to be more fully addressed.

Conflict of Interest

The results from this study involve no financial conflicts of interest for either author, both of whom work at the University of Michigan. There is no other affiliation for either author that may be perceived as having a conflict of interest with respect to the results of this paper.

Data Availability Statement

Data sets for the research discussed in this study (primarily results of microprobe analyses) are included in this paper (and its supporting information files). Additionally, all data are currently archived in the EarthChem data repository (https://doi.org/10.26022/IEDA/111589).

References

Allan, J. F., Batiza, R., Perfit, M. R., Fornari, D. J., & Sack, R. O. (1989). Petrology of lavas from the Lamont seamount chain and adjacent East Pacific Rise, 10°N. *Journal of Petrology*, *30*(5), 1245–1298. https://doi.org/10.1093/petrology/30.5.1245

Almeev, R. R., Holtz, F., Koepke, J., Parat, F., & Botcharnikov, R. E. (2007). The effect of H_2O on olivine crystallization in MORB: Experimental calibration at 200 MPa. *American Mineralogist*, *92*(4), 670–674. https://doi.org/10.2138/am.2007.2484

Asimow, P. D., & Ghiorso, M. S. (1998). Algorithmic modifications extending MELTS to calculate subsolidus phase relations. *American Mineralogist*, *83*(9–10), 1127–1132. https://doi.org/10.2138/am-1998-9-1022

Asimow, P. D., Hirshmann, M. M., & Stolper, E. M. (2001). Calculation of peridotite partial melting from thermodynamic models of minerals and melts, IV. Adiabatic decompression and the composition and mean properties of mid-ocean ridge basalts. *Journal of Petrology*, *42*(5), 963–998. https://doi.org/10.1093/petrology/42.5.963

Bacon, C. R., & Hirschmann, M. M. (1988). Mg/Mn partitioning as a test for equilibrium between coexisting Fe-Ti oxides. *American Mineralogist*, *73*(Table l), 57–61.

Beard, B. L., & Glazner, A. F. (1995). Trace element and Sr and Nd isotopic composition of mantle xenoliths from the Big Pine volcanic field, California. *Journal of Geophysical Research*, *100*(B3), 4169–4179. https://doi.org/10.1029/94JB02883

Beard, B. L., & Johnson, C. M. (1997). Hafnium isotope evidence for the origin of Cenozoic basaltic lavas from the southwestern United States. *Journal of Geophysical Research*, *102*(B9), 20,149–20,178. https://doi.org/10.1029/97JB01731

Beattie, P. (1993). Olivine-melt and orthopyroxene-melt equilibria. *Contributions to Mineralogy and Petrology*, *115*(1), 103–111. https://doi.org/10.1007/BF00712982

Blondes, M. S., Reiners, P. W., Ducea, M. N., Singer, B. S., & Chesley, J. (2008). Temporal-compositional trends over short and long time-scales in basalts of the Big Pine Volcanic Field, California. *Earth and Planetary Science Letters*, *269*(1–2), 140–154. https://doi.org/10.1016/j.epsl.2008.02.012

Blondes, M. S., Reiners, P. W., Edwards, B. R., & Biscontini, A. (2007). Dating young basalt eruptions by (U-Th)/He on xenolithic zircons. *Geology*, *35*(1), 17–20. https://doi.org/10.1130/G22956A.1

Brophy, J. G., Whittington, C. S., & Park, Y. R. (1999). Sector-zoned augite megacrysts in Aleutian high alumina basalts: Implications for the conditions of basalt crystallization and the generation of calc-alkaline series magmas. *Contributions to Mineralogy and Petrology*, *135*(2–3), 277–290. https://doi.org/10.1007/s004100050512

Christiansen, R. L., & Lipman, P. W. (1972). Cenozoic volcanism and plate-tectonic evolution of the western United States. II. Late Cenozoic. *Philosophical Transactions of the Royal Society of London A: Mathematical, Physical and Engineering Sciences*, *271*(1213), 249–284. https://doi.org/10.1098/rsta.1972.0009

Colgan, J. P., Dumitru, T. A., Reiners, P. W., Wooden, J. L., & Miller, E. L. (2006). Cenozoic tectonic evolution of the basin and range province in northwestern Nevada. *American Journal of Science*, *306*(8), 616–654. https://doi.org/10.2475/08.2006.02

Crabtree, S. M., & Lange, R. A. (2012). An evaluation of the effect of degassing on the oxidation state of hydrous andesite and dacite magmas: A comparison of pre- and post-eruptive Fe^{2+} concentrations. *Contributions to Mineralogy and Petrology*, *163*(2), 209–224. https://doi.org/10.1007/s00410-011-0667-7

DePaolo, D. J., & Daley, E. E. (2000). Neodymium isotopes in basalts of the southwest basin and range and lithospheric thinning during continental extension. *Chemical Geology*, *169*(1–2), 157–185. https://doi.org/10.1016/S0009-2541(00)00261-8

Ducea, M. N., & Saleeby, J. B. (1996). Buoyancy sources for a large, unrooted mountain range, the Sierra Nevada, California; evidence from xenolith thermobarometry. *Journal of Geophysical Research*, *101*(B4), 8229–8244. https://doi.org/10.1029/95JB03452

Gavrilenko, M., Herzberg, C., Vidito, C., Carr, M. J., Tenner, T., & Ozerov, A. (2016). A calcium-in-olivine geohygrometer and its application to subduction zone magmatism. *Journal of Petrology*, *57*(9), 1811–1832. https://doi.org/10.1093/petrology/egw062

Gazel, E., Plank, T., Forsyth, D. W., Bendersky, C., Lee, C. T. A., & Hauri, E. H. (2012). Lithosphere versus asthenosphere mantle sources at the Big Pine Volcanic Field, California. *Geochemistry, Geophysics, Geosystems*, *13*, Q0AK06. https://doi.org/10.1029/2012GC004060

Ghiorso, M. S., & Evans, B. W. (2008). Thermodynamics of rhombohedral oxide solid solutions and a revision of the Fe-Ti two-oxide geothermometer and oxygen-barometer. *American Journal of Science*, *308*(9), 957–1039. https://doi.org/10.2475/09.2008.01

Ghiorso, M. S., & Sack, R. O. (1995). Chemical mass transfer in magmatic processes IV. A revised and internally consistent thermodynamic model for the interpolation and extrapolation of liquid-solid equilibria in magmatic systems at elevated temperatures and pressures. *Contributions to Mineralogy and Petrology*, *119*(2–3), 197–212. https://doi.org/10.1007/BF00307281

Haase, C. S., Chadam, J., Feinn, D., & Ortoleva, P. (1980). Oscillatory zoning in plagioclase feldspar. *Science*, *209*(4453), 272–274. https://doi.org/10.1126/science.209.4453.272

Hammer, J., Jacob, S., Welsch, B., Hellebrand, E., & Sinton, J. (2016). Clinopyroxene in postshield Haleakala ankaramite: 1. Efficacy of thermobarometry. *Contributions to Mineralogy and Petrology*, *171*, 7–23. https://doi.org/10.1007/s00410-015-1212-x

Henry, C. D., & Perkins, M. E. (2002). Sierra Nevada–Basin and Range transition near Reno, Nevada: Two-stage development at 12 and 3 Ma. *Geology*, *29*(8), 719–722. https://doi.org/10.1130/0091-7613(2001)029<0719:SNBART>2.0.CO;2

Herzberg, C., & Asimow, P. D. (2008). Petrology of some oceanic island basalts: PRIMELT2.XLS software for primary magma calculation. *Geochemistry, Geophysics, Geosystems*, *9*, Q09001. https://doi.org/10.1029/2008GC002057

Hofmann, A. W., & Jochum, K. P. (1996). Source characteristics derived from very incompatible trace elements in Mauna Loa and Mauna Kea basalts, Hawaii Scientific Drilling Project. *Journal of Geophysical Research*, *101*(B5), 11,831–11,839. https://doi.org/10.1029/95JB03701

Housh, T. B., Aranda-Gómez, J. J., & Luhr, J. F. (2010). Isla Isabel (Nayarit, México): Quaternary alkalic basalts with mantle xenoliths erupted in the mouth of the Gulf of California. *Journal of Volcanology and Geothermal Research*, *197*(1–4), 85–107. https://doi.org/10.1016/j.jvolgeores.2009.06.011

Johnson, E. R., Wallace, P. J., Cashman, K. V., Granados, H. D., & Kent, A. J. R. (2008). Magmatic volatile contents and degassing-induced crystallization at Volcán Jorullo, Mexico: Implications for melt evolution and the plumbing systems of monogenetic volcanoes. *Earth and Planetary Science Letters*, *269*(3–4), 478–487. https://doi.org/10.1016/j.epsl.2008.03.004

Johnson, E. R., Wallace, P. J., Delgado Granados, H., Manea, V. C., Kent, A. J. R., Bindeman, I. N., & Donegan, C. S. (2009). Subduction-related volatile recycling and magma generation beneath Central Mexico: Insights from melt inclusions, oxygen isotopes and geodynamic models. *Journal of Petrology*, *50*(9), 1729–1764. https://doi.org/10.1093/petrology/egp051

Kelley, K. A., & Cottrell, E. (2012). The influence of magmatic differentiation on the oxidation state of Fe in a basaltic arc magma. *Earth and Planetary Science Letters*, *329–330*, 109–121. https://doi.org/10.1016/j.epsl.2012.02.010

Kistler, R. W. (1990). Chapter 15: Two different lithosphere types in the Sierra Nevada, California. In J. L. Anderson (Ed.), *The nature and origin of Cordilleran magmatism* (Vol. 174, pp. 271–281). Geological Society of America. https://doi.org/10.1130/MEM174-p271

Kouchi, A., Sugawara, Y., Kashima, K., & Sunagawa, I. (1983). Laboratory growth of sector zones clinopyroxenes in the system $CaMgSi_2O_6$-$CaTiAl_2O_6$. *Contributions to Mineralogy and Petrology*, *83*(1–2), 177–184. https://doi.org/10.1007/BF00373091

L'Heureux, I. (1993). Oscillatory zoning in crystal growth: A constitutional undercooling mechanism. *Physical Review E*, *48*(6), 4460–4469. https://doi.org/10.1103/PhysRevE.48.4460

Lee, C. T., Rudnick, R. L., & Brimhall, G. H. (2001). Deep lithospheric dynamics beneath the Sierra Nevada during the Mesozoic and Cenozoic as inferred from xenolith petrology. *Geochemistry, Geophysics, Geosystems*, *2*(12), 1053. https://doi.org/10.1029/2001GC000152

Lipman, P. W., Prostka, H. J., & Christiansen, R. L. (1972). Cenozoic volcanism and plate-tectonic evolution of the western United States. I. Early and middle Cenozoic. *Philosophical Transactions of the Royal Society of London. Series A, Mathematical and Physical Sciences*, *271*(1213), 217–248.

Lofgren, G. (1974). An experimental study of plagioclase crystal morphology: Isothermal crystallization. *American Journal of Science*, *274*(3), 243–273. https://doi.org/10.2475/ajs.274.3.243

McDonough, W. F., & Sun, S. S. (1995). The composition of the Earth. *Chemical Geology*, *120*, 223–253. https://doi.org/10.1016/0009-2541(94)00140-4

McKenzie, D., & Bickle, M. J. (1988). The volume and composition of melt generated by extension of the lithosphere. *Journal of Petrology*, *29*(3), 625–679. https://doi.org/10.1093/petrology/29.3.625

Médard, E., & Grove, T. L. (2008). The effect of H_2O on the olivine liquidus of basaltic melts: Experiments and thermodynamic models. *Contributions to Mineralogy and Petrology*, *155*(4), 417–432. https://doi.org/10.1007/s00410-007-0250-4

Milman-Barris, M. S., Beckett, J. R., Baker, M. B., Hofmann, A. E., Morgan, Z., Crowley, M. R., & Stolper, E. (2008). Zoning of phosphorus in igneous olivine. *Contributions to Mineralogy and Petrology*, *155*(6), 739–765. https://doi.org/10.1007/s00410-007-0268-7

Mollo, S., Ubide, T., Di Stefano, F., Nazzari, M., & Scarlato, P. (2020). Polybaric/polythermal magma transport and trace element partitioning recorded in single crystals: A case study of a zoned clinopyroxene from Mt. Etna. *Lithos*, *356*, 105382. https://doi.org/10.1016/j.lithos.2020.105382

Mordick, B. E., & Glazner, A. F. (2006). Clinopyroxene thermobarometry of basalts from the Coso and Big Pine volcanic fields, California. *Contributions to Mineralogy and Petrology*, *152*(1), 111–124. https://doi.org/10.1007/s00410-006-0097-0

Neave, D. A., & Putirka, K. D. (2017). A new clinopyroxene-liquid barometer, and implications for magma storage pressures under Icelandic rift zones. *American Mineralogist*, *102*(4), 777–794. https://doi.org/10.2138/am-2017-5968

Norman, M. D., & Garcia, M. O. (1999). Primitive magmas and source characteristics of the Hawaiian plume: Petrology and geochemistry of shield picrites. *Earth and Planetary Science Letters*, *168*(1–2), 27–44. https://doi.org/10.1016/S0012-821X(99)00043-6

Ormerod, D. S., Hawkesworth, C. J., Rogers, N. W., Leeman, W. P., & Menzies, M. A. (1988). Tectonic and magmatic transitions in the Western Great Basin, USA. *Nature*, *333*(6171), 349–353. https://doi.org/10.1038/333349a0

Ormerod, D. S., Rogers, N. W., & Hawkesworth, C. J. (1991). Melting in the lithospheric mantle: Inverse modelling of alkali-olivine basalts from the Big Pine Volcanic California. *Contributions to Mineralogy and Petrology*, *108*(3), 305–317. https://doi.org/10.1007/BF00285939

Plank, T., & Forsyth, D. W. (2016). Thermal structure and melting conditions in the mantle beneath the Basin and Range province from seismology and petrology. *Geochemistry, Geophysics, Geosystems*, *17*, 1312–1338. https://doi.org/10.1002/2015GC006205

Pu, X. (2018). *New constraints on temperature, oxygen fugacity, and H_2O of subduction zone basalts based on olivine-melt equilibrium* (Doctoral dissertation). Ann Arbor, USA: University of Michigan. Retrieved from https://deepblue.lib.umich.edu/handle/2027.42/144078

Pu, X., Lange, R. A., & Moore, G. (2017). A comparison of olivine-melt thermometers based on DMg and DNi: The effects of melt composition, temperature, and pressure with applications to MORBs and hydrous arc basalts. *American Mineralogist*, *102*(4), 750–765. https://doi.org/10.2138/am-2017-5879

Putirka, K. (2008). Excess temperatures at ocean islands: Implications for mantle layering and convection. *Geology*, *36*(4), 283–286. https://doi.org/10.1130/G24615A.1

Putirka, K., Jean, M., Cousens, B., Sharma, R., Torrez, G., & Carlson, C. (2012). Cenozoic volcanism in the Sierra Nevada and Walker Lane, California, and a new model for lithosphere degradation. *Geosphere*, *8*(2), 265–291. https://doi.org/10.1130/GES00728.1

Putirka, K., Tao, Y., Hari, K. R., Perfit, M. R., Jackson, M. G., & Arevalo, R. (2018). The mantle source of thermal plumes: Trace and minor elements in olivine and major oxides of primitive liquids (and why the olivine compositions don't matter). *American Mineralogist*, *103*(8), 1253–1270. https://doi.org/10.2138/am-2018-6192

Putirka, K. D. (2005). Mantle potential temperatures at Hawaii, Iceland, and the mid-ocean ridge system, as inferred from olivine phenocrysts: Evidence for thermally driven mantle plumes. *Geochemistry, Geophysics, Geosystems*, *6*, Q05L08. https://doi.org/10.1029/2005GC000915

Putirka, K. D. (2016). Rates and styles of planetary cooling on Earth, Moon, Mars, and Vesta, using new models for oxygen fugacity, ferric-ferrous ratios, olivine-liquid Fe-Mg exchange, and mantle potential temperature. *American Mineralogist*, *101*(Korenaga 2008), 819–840. https://doi.org/10.2138/am-2016-5402

Putirka, K. D., Perfit, M., Ryerson, F. J., & Jackson, M. G. (2007). Ambient and excess mantle temperatures, olivine thermometry, and active vs. passive upwelling. *Chemical Geology*, *241*(3–4), 177–206. https://doi.org/10.1016/j.chemgeo.2007.01.014

Reiners, P. W., Hammond, P. E., McKenna, J. M., & Duncan, R. A. (2000). Young basalts of the central Washington Cascades, flux melting of the mantle, and trace element signatures of primary arc magmas. *Contributions to Mineralogy and Petrology*, *138*(3), 249–264. https://doi.org/10.1007/s004100050561

Roeder, P. L., Poustovetov, A., & Oskarsson, N. (2001). Growth forms and composition of chromian spinel in MORB magma: Diffusion-controlled crystallization of chromian spinel. *Canadian Mineralogist*, *39*(2), 397–416. https://doi.org/10.2113/gscanmin.39.2.397

Shea, T., Hammer, J. E., Hellebrand, E., Mourey, A. J., Costa, F., First, E. C., et al. (2019). Phosphorous and aluminum zoning in olivine: Contrasting behavior of two nominally incompatible trace elements. *Contributions to Mineralogy and Petrology*, *174*(85), 1–24.

Shimizu, N. (1990). The oscillatory trace element zoning of augite phenocrysts. *Earth Science Reviews*, *29*(1–4), 27–37. https://doi.org/10.1016/0012-8252(0)90025-Q

Simkin, T. O. M., & Smith, J. V. (1970). Minor-element distribution in olivine. *The Journal of Geology*, *78*(3), 304–325. https://doi.org/10.1086/627519

Skulski, T., Minarik, W., & Watson, E. B. (1994). High-pressure experimental trace-element partitioning between clinopyroxene and basaltic melts. *Chemical Geology*, *117*(1–4), 127–147. https://doi.org/10.1016/0009-2541(94)90125-2

Snyder, W. S., Dickinson, W. R., & Silberman, M. L. (1976). Tectonic implications of space-time patterns of Cenozoic magmatism in the western United States. *Earth and Planetary Science Letters*, *32*(1), 91–106.

Sparks, R. S. J., Pinkerton, H., & MacDonald, R. (1977). The transport of xenoliths in magmas. *Earth and Planetary Science Letters*, *35*(2), 234–238. https://doi.org/10.1016/0012-821X(77)90126-1

Spera, F. J. (1980). In R. B. Hargraves (Ed.), *Aspects of magma transport in physics of magmagtic processes* (pp. 265–323). Princeton, NJ: Princeton University Press.

Spera, F. J. (1984). Carbon dioxide in petrogenesis III: Role of volatiles in the ascent of alkaline magma with special reference to xenolith-bearing mafic lavas. *Contributions to Mineralogy and Petrology*, *88*(3), 217–232. https://doi.org/10.1007/BF00380167

Stockli, D. F., Dumitru, T. A., McWilliams, M. O., & Farley, K. A. (2003). Cenozoic tectonic evolution of the White Mountains, California and Nevada. *GSA Bulletin*, *115*(7), 788–816. https://doi.org/10.1130/0016-7606(2003)115<0788:CTEOTW>2.0.CO;2

Ubide, T., Mollo, S., Zhao, J., Xin Nazzari, M., & Scarlato, P. (2019). Sector-zoned clinopyroxene as a recorder of magma history, eruption triggers, and ascent rates. *Geochimica et Cosmochimica Acta*, *251*, 265–283. https://doi.org/10.1016/j.gca.2019.02.021

Vazquez, J. A., & Woolford, J. M. (2015). Late Pleistocene ages for the most recent volcanism and glacial-pluvial deposits at Big Pine volcanic field, California, USA, from cosmogenic ^{36}Cl dating. *Geochemistry, Geophysics, Geosystems*, *16*, 2812–2828. https://doi.org/10.1002/2015GC005889

Waters, L. E., & Lange, R. A. (2015). An updated calibration of the plagioclase-liquid hygrometer-thermometer applicable to basalts through rhyolites. *American Mineralogist*, *100*(10), 2172–2184. https://doi.org/10.2138/am-2015-5232

Waters, L. E., & Lange, R. A. (2016). No effect of H_2O degassing on the oxidation state of magmatic liquids. *Earth and Planetary Science Letters*, *447*, 48–59. https://doi.org/10.1016/j.epsl.2016.04.030

Weaver, S. L., Wallace, P. J., & Johnston, A. D. (2011). A comparative study of continental vs. intraoceanic arc mantle melting: Experimentally determined phase relations of hydrous primitive melts. *Earth and Planetary Science Letters*, *308*(1–2), 97–106. https://doi.org/10.1016/j.epsl.2011.05.040

Welsch, B., Faure, F., Famin, V., Baronnet, A., & Bachèlery, P. (2012). Dendritic crystallization: A single process for all the textures of olivine in basalts? *Journal of Petrology*, *54*(3), 539–574. https://doi.org/10.1093/petrology/egs077

Welsch, B., Hammer, J., Baronnet, A., Jacob, S., Hellebrand, E., & Sinton, J. (2016). Clinopyroxene in postshield Haleakala ankaramite: 2. Texture, compositional zoning and supersaturation in the magma. *Contributions to Mineralogy and Petrology*, *171*(1), 6–19. https://doi.org/10.1007/s00410-015-1213-9

Welsch, B., Hammer, J., & Hellebrand, E. (2014). Phosphorus zoning reveals dendritic architecture of olivine. *Geology*, *42*(10), 867–870. https://doi.org/10.1130/G35691.1

Wilshire, H., Meyer, C. E., Nakata, J. K., & Calk, L. C. (1988). *Mafic and ultramafic xenoliths from volcanic rocks of the western United States*. Washington, DC: U.S. Geological Survey. https://doi.org/10.3133/ofr85139

Wilson, A. D. (1960). The micro-determination of ferrous iron in silicate minerals by a volumetric and a colorimetric method. *Analyst*, *85*(1016), 823–827. https://doi.org/10.1039/an9608500823